2018

Loss of Dnmt3a immortalizes hematopoietic stem cells in vivo

Mira Jeong
Baylor College of Medicine

Hyun Jung Park
Baylor College of Medicine

Hamza Celik
Washington University School of Medicine in St. Louis

Elizabeth L. Ostrander
Washington University School of Medicine in St. Louis

Jaime M. Reyes
Baylor College of Medicine

See next page for additional authors

Report

Cell Reports

Loss of Dnmt3a Immortalizes Hematopoietic Stem Cells *In Vivo*

Graphical Abstract

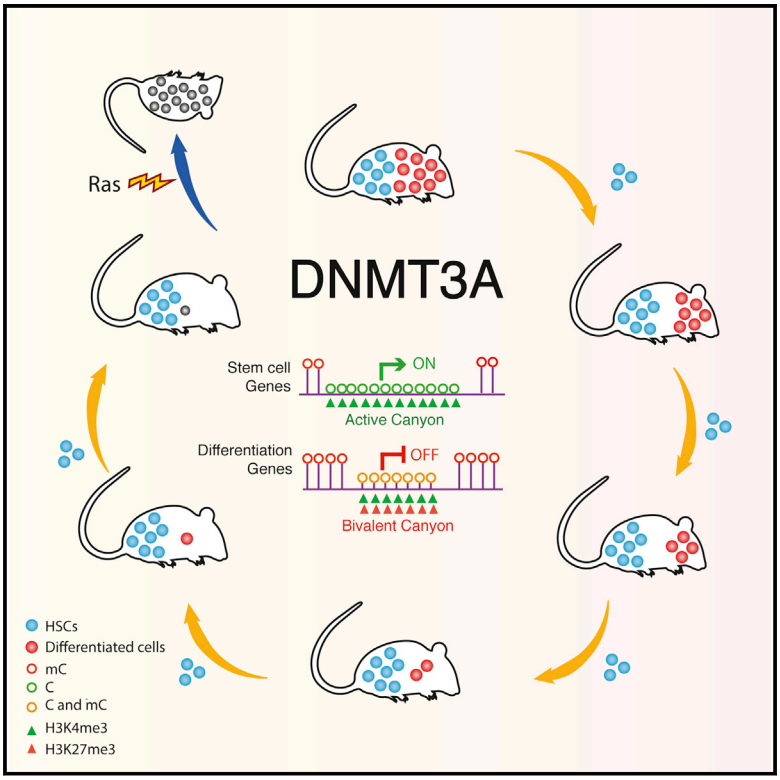

Authors

Mira Jeong, Hyun Jung Park, Hamza Celik, ..., Wei Li, Margaret A. Goodell, Grant A. Challen

Correspondence

goodell@bcm.edu (M.A.G.), gchallen@dom.wustl.edu (G.A.C.)

In Brief

Jeong et al. show that a single genetic manipulation, conditional inactivation of the DNA methyltransferase enzyme Dnmt3a, removes all inherent hematopoietic stem cell (HSC) self-renewal limits and replicative lifespan. Deletion of *Dnmt3a* allows HSCs to be propagated indefinitely *in vivo*.

Highlights

- Serial propagation of HSCs for 12 transplant generations, over 60 months *in vivo*
- Augmentation of modifications at enhancers and canyons to buttress self-renewal
- Differentiation becomes irreversibly compromised, but transformation potential remains

Data and Software Availability

GSE98191

Jeong et al., 2018, Cell Reports *23*, 1–10
April 3, 2018
https://doi.org/10.1016/j.celrep.2018.03.025

CellPress

Cell Reports
Report

Loss of Dnmt3a Immortalizes Hematopoietic Stem Cells *In Vivo*

Mira Jeong,[1,9] Hyun Jung Park,[2,9] Hamza Celik,[3,9] Elizabeth L. Ostrander,[3] Jaime M. Reyes,[4] Anna Guzman,[1] Benjamin Rodriguez,[2] Yong Lei,[1] Yeojin Lee,[5] Lei Ding,[5] Olga A. Guryanova,[6] Wei Li,[2,7] Margaret A. Goodell,[1,4,*] and Grant A. Challen[3,8,10,*]

[1]Stem Cells and Regenerative Medicine Center, Baylor College of Medicine, Houston, TX 77030, USA
[2]Dan L. Duncan Cancer Center, Baylor College of Medicine, Houston, TX 77030, USA
[3]Division of Oncology, Department of Medicine, Washington University School of Medicine, St. Louis, MO 63110, USA
[4]Department of Molecular and Human Genetics, Baylor College of Medicine, Houston, TX 77030, USA
[5]Columbia Stem Cell Initiative, Department of Rehabilitation and Regenerative Medicine, Department of Microbiology and Immunology, Columbia University Medical Center, New York, NY 10032, USA
[6]Department of Pharmacology and Therapeutics, University of Florida College of Medicine, and UF Health Cancer Center, Gainesville, FL 32610, USA
[7]Department of Molecular and Cellular Biology, Baylor College of Medicine, Houston, TX 77030, USA
[8]Developmental, Regenerative and Stem Cell Biology Program, Division of Biology and Biomedical Sciences, Washington University School of Medicine, St. Louis, MO 63110, USA
[9]These authors contributed equally
[10]Lead Contact
*Correspondence: goodell@bcm.edu (M.A.G.), gchallen@dom.wustl.edu (G.A.C.)
https://doi.org/10.1016/j.celrep.2018.03.025

SUMMARY

Somatic mutations in *DNMT3A* are recurrent events across a range of blood cancers. *Dnmt3a* loss of function in hematopoietic stem cells (HSCs) skews divisions toward self-renewal at the expense of differentiation. Moreover, *DNMT3A* mutations can be detected in the blood of aging individuals, indicating that mutant cells outcompete normal HSCs over time. It is important to understand how these mutations provide a competitive advantage to HSCs. Here we show that *Dnmt3a*-null HSCs can regenerate over at least 12 transplant generations in mice, far exceeding the lifespan of normal HSCs. Molecular characterization reveals that this *in vivo* immortalization is associated with gradual and focal losses of DNA methylation at key regulatory regions associated with self-renewal genes, producing a highly stereotypical HSC phenotype in which epigenetic features are further buttressed. These findings lend insight into the preponderance of *DNMT3A* mutations in clonal hematopoiesis and the persistence of mutant clones after chemotherapy.

INTRODUCTION

Embryonic stem cells (ESCs) can be propagated indefinitely *in vitro* while maintaining their defining stem cell properties of self-renewal and differentiation. However, self-renewal of somatic stem cells such as hematopoietic stem cells (HSCs) appears to have a limit, as serial transplantation invariably results in loss of repopulation ability (Micklem et al., 1987; Siminovitch et al., 1964; Harrison and Astle, 1982). Understanding these limitations is important for dissecting stem cell regulation and developing strategies to expand HSCs *ex vivo* for cell and gene therapy applications.

We previously showed that genetic inactivation of de novo DNA methyltransferase 3a (*Dnmt3a*) enhances self-renewal of murine HSCs (Challen et al., 2011, 2014). In humans, mutations in *DNMT3A* have been associated with clonal hematopoiesis of indeterminate potential (CHIP) in aging individuals (Genovese et al., 2014; Jaiswal et al., 2014; Xie et al., 2014). *DNMT3A* mutations in CHIP typically result in loss of activity through divergent mechanisms (Kim et al., 2013; Russler-Germain et al., 2014; Spencer et al., 2017), which probably confers enhanced self-renewal and enables them to slowly outcompete their normal counterparts over a long timescale.

Although loss of *Dnmt3a* promotes self-renewal, the degree of enhancement is undefined. Given that *DNMT3A* mutations are frequent in hematologic malignancies (Yang et al., 2015), are associated with a pre-malignant state (Shlush et al., 2014; Corces-Zimmerman et al., 2014), and can repopulate after chemotherapy (Pløen et al., 2014), it is critical to understand the mechanisms of resilience and longevity of *DNMT3A* mutant HSCs. Here we rigorously examine the replicative limits of HSCs lacking *Dnmt3a*.

RESULTS

Loss of Dnmt3a Provides HSCs with Indefinite Longevity

We previously showed that *Dnmt3a*-null (Mx1-Cre:*Dnmt3a*$^{fl/fl}$ HSCs treated with pIpC = *Dnmt3a*^{KO}) HSCs could self-renew for up to four rounds of serial transplantation (Challen et al., 2011). We terminated these experiments after four transplants because control HSCs failed to self-renew past this point. However, as *Dnmt3a*^{KO} HSCs continued to show robust HSC

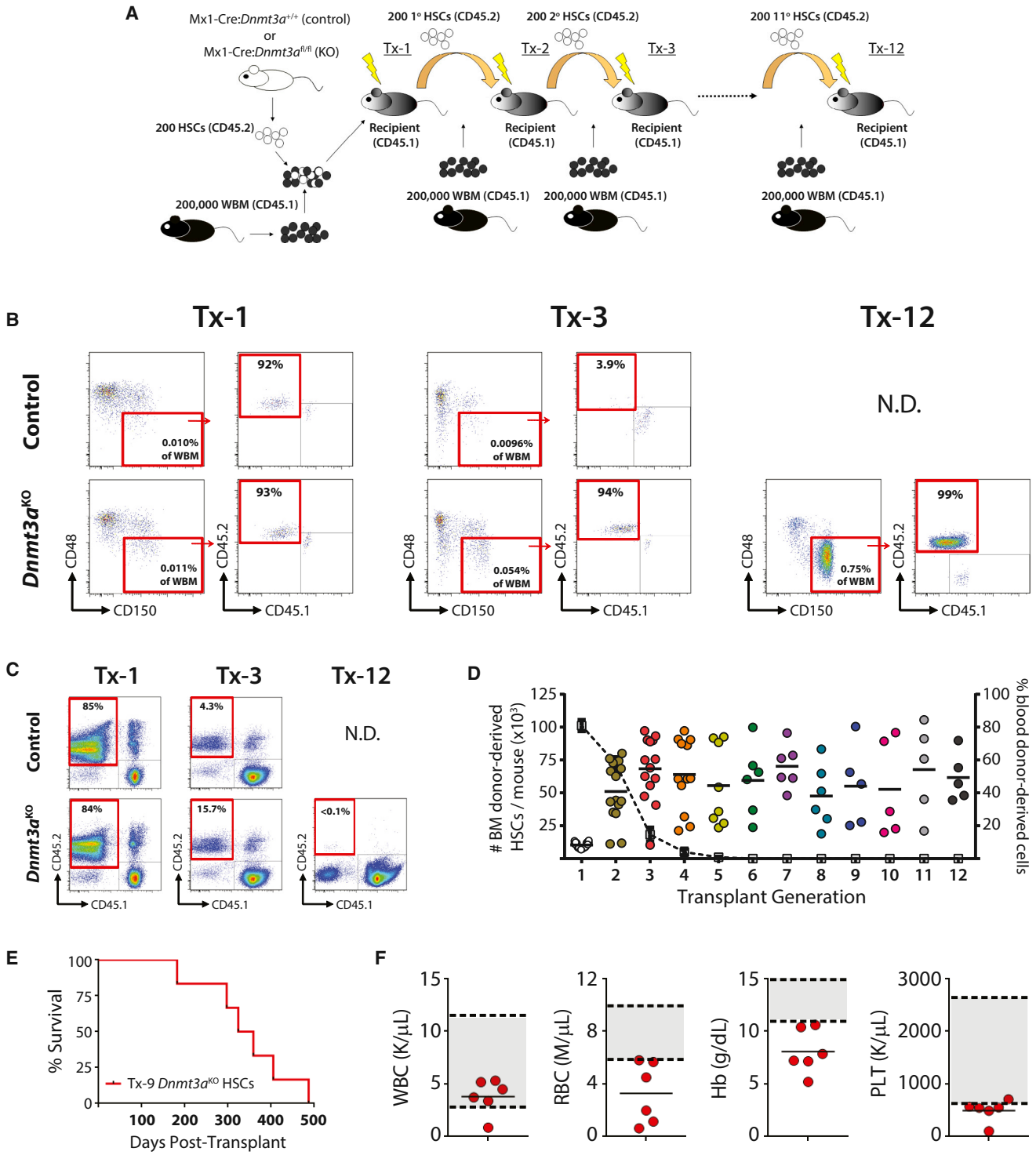

Figure 1. Loss of *Dnmt3a* Provides HSCs with Indefinite Longevity

(A) Schematic representation of serial HSC transplantation process. Tx, transplant stage; HSCs, hematopoietic stem cells; WBM, whole bone marrow.

(B and C) Representative flow cytometry plots showing donor-derived cell ($CD45.2^+$) contribution to bone marrow HSC compartment (B) and peripheral blood (C) at the end of indicated stage of transplantation. N.D., not determined.

(legend continued on next page)

repopulation, we hypothesized that *Dnmt3a* loss of function may remove inherent constraints on HSC self-renewal and longevity. Here, we tested these limits. Phenotypic HSCs (Lineage$^-$ c-Kit$^+$ Sca-1$^+$ CD48$^-$ CD150$^+$ CD45.2$^+$) were purified from prior recipients (CD45.1$^+$) using flow cytometry. Two hundred HSCs were re-injected along with fresh whole bone marrow (WBM) competitor cells (CD45.1$^+$) into new recipients (Figure 1A). Eighteen to 24 weeks later, recipients were sacrificed for analysis and continued HSC transplantation. After each transplant round, donor-derived (CD45.2$^+$) HSCs were quantified (Figure 1B). After the third transplant, *Dnmt3a*^{KO} HSCs failed to generate substantial peripheral blood progeny (Figures 1C and 1D). Nevertheless, robust repopulation of *Dnmt3a*^{KO} HSCs was readily detectable in the bone marrow of recipient mice over 12 rounds of transplantation (Figure 1D). These HSCs displayed all the canonical markers of long-term HSCs (Figure S1A), and the expanded population was highly restricted to the HSC pool (Figure S1B). This degree of self-renewal far exceeds the potential of normal HSCs.

When *Dnmt3a*^{KO} HSCs are forced to differentiate in the absence of WBM competitor cells, a variety of hematopoietic pathologies arise (Celik et al., 2015; Mayle et al., 2015). To determine whether the immortalized HSCs were transformed, we transplanted 1 × 10^5 ninth-generation transplant (Tx-9) *Dnmt3a*^{KO} HSCs without competitor WBM. These animals succumbed to bone marrow failure (Figure 1E) with anemia and peripheral cytopenias (Figure 1F), likely resulting from the inability of *Dnmt3a*^{KO} HSCs to generate sufficient blood elements to sustain the recipients in the absence of wild-type (WT) support cells. Bone marrow histology (data not shown) showed no evidence of leukemic transformation. Expanded *Dnmt3a*^{KO} HSCs were not mobilized in the blood (Figure S1C), and no extramedullary hematopoiesis was observed in the spleen (Figure S1D). Mice transplanted with control or *Dnmt3a*^{KO} HSCs contained similar numbers of stromal cells (Figure S1E) and appropriate bone marrow localization (Figure S1F). *Dnmt3a*^{KO} HSCs showed similar proximity to endothelial cells as control HSCs (Figure S1G) but were found to be closer to neighboring HSCs (Figure S1H), as would be expected from their clonal expansion.

Dnmt3a Controls DNA Methylation at HSC Regulatory Elements

We performed molecular comparisons of age-matched control and early-stage transplant *Dnmt3a*^{KO} HSCs with late-stage transplant *Dnmt3a*^{KO} HSCs. Global DNA methylation analysis (Figure S2A; Table S1) showed that Tx-11 *Dnmt3a*^{KO} HSCs retained their overall methylation profile, with the majority of CpGs still methylated throughout the genome, but displayed DNA hypomethylation compared with control HSCs. This pattern was similar to, but more exaggerated than, the depletion of DNA methylation in early-stage transplant (Tx-3) *Dnmt3a*^{KO} HSCs (Figure 2A).

Differentially methylated regions (DMRs) were defined as more than three CpGs within 300 bp that show >20% methylation change in the same direction. Of the genomic regions showing differential methylation both in Tx-3 *Dnmt3a*^{KO} (to age-matched WT) and Tx-11 *Dnmt3a*^{KO} (versus Tx-3) HSCs, 556 regions hypermethylated in Tx-3 were equally as likely to gain (297) or lose (259) DNA methylation in Tx-11 *Dnmt3a*^{KO} HSCs (Figure 2B), suggesting that this hypermethylation was not stable. Conversely, 4,313 of 4,986 regions (86.5%) of the genome that lost DNA methylation in early-passage *Dnmt3a*^{KO} HSCs (hypo-DMRs) showed a trend toward continued loss of methylation in later stage transplant *Dnmt3a*^{KO} HSCs. There was significant enrichment for these "hypo_hypo" DMRs in stem cell enhancer elements (Figure 2C), but not CpG islands or gene promoters. "Hypo_hypo" DMRs were also enriched for transcription factor binding sites (TFBSs; Figure S2B), including hematopoietic regulators such as Gata2 (Figure S2C). This enrichment was not due to the difference in DMR numbers, as 100 random computational samplings of 600 "hypo_hypo" and "hypo_hyper" DMRs showed the same trend (Figure S2D).

Because loss of DNA methylation in *Dnmt3a*^{KO} HSCs is particularly concentrated in DNA methylation canyons (Jeong et al., 2014), we examined canyons in late-passage HSCs. There are 1,093 canyons in WT HSCs (Jeong et al., 2014), which can be subdivided on the basis of histone marks into 565 active (H3K4me3$^+$), 205 bivalent (H3K4me3$^+$ H3K27me3$^+$), and 323 inactive (H3K27me3$^+$) canyons. Targeted loss of DNA methylation at active canyon walls was previously noted in early-passage *Dnmt3a*^{KO} HSCs (Jeong et al., 2014). In Tx-11 *Dnmt3a*^{KO} HSCs, there was further erosion of these walls (Figure 2D), and hypomethylation extended from the canyon edges (Figure S2E). In contrast, bivalent and inactive canyons displayed increased DNA methylation in Tx11 *Dnmt3a*^{KO} HSCs (Figure 2E) and no changes in the canyon border region (Figure S2E). Hypermethylation of inactive canyons did not lead to altered gene expression, as these genes are typically expressed at negligible levels (Figure 2F). However, genes in bivalent canyons, exemplified by *Cxcl12* (Figure 2E), showed repression following hypermethylation with extended passage. As many genes contained in such canyons are important for HSC lineage commitment, this hypermethylation may be a mechanism that inhibits differentiation of the mutant HSCs.

RNA sequencing (RNA-seq) was performed to determine the impact of DNA methylation changes on gene expression. In general, genes that were differentially expressed between control and Tx-3 *Dnmt3a*^{KO} HSCs showed similar expression patterns in Tx-9 *Dnmt3a*^{KO} HSCs (Figure S2F). We noted previously that early-passage *Dnmt3a*^{KO} HSCs exhibited increased expression of genes associated with HSC identity (Challen et al., 2011), defined as "HSC fingerprint" genes (Chambers et al., 2007). This trend continued in Tx-9 *Dnmt3a*^{KO} HSCs. Although the majority of HSC fingerprint genes are upregulated in mutant HSCs,

(D) Quantification of donor HSC-derived peripheral blood chimerism (dashed gray line) compared with absolute number of donor-derived HSCs per mouse generated from *Dnmt3a*^{KO} HSCs at the end of each transplant (n = 5–29 recipients per transplant generation).
(E) Time to morbidity in mice transplanted with 1 × 10^5 *Dnmt3a*^{KO} HSCs in the absence of WBM competitor cells.
(F) Blood counts from moribund mice showing leukopenia, anemia, and thrombocytopenia. Gray shaded areas indicate normal range for WT mice.
See also Figure S1.

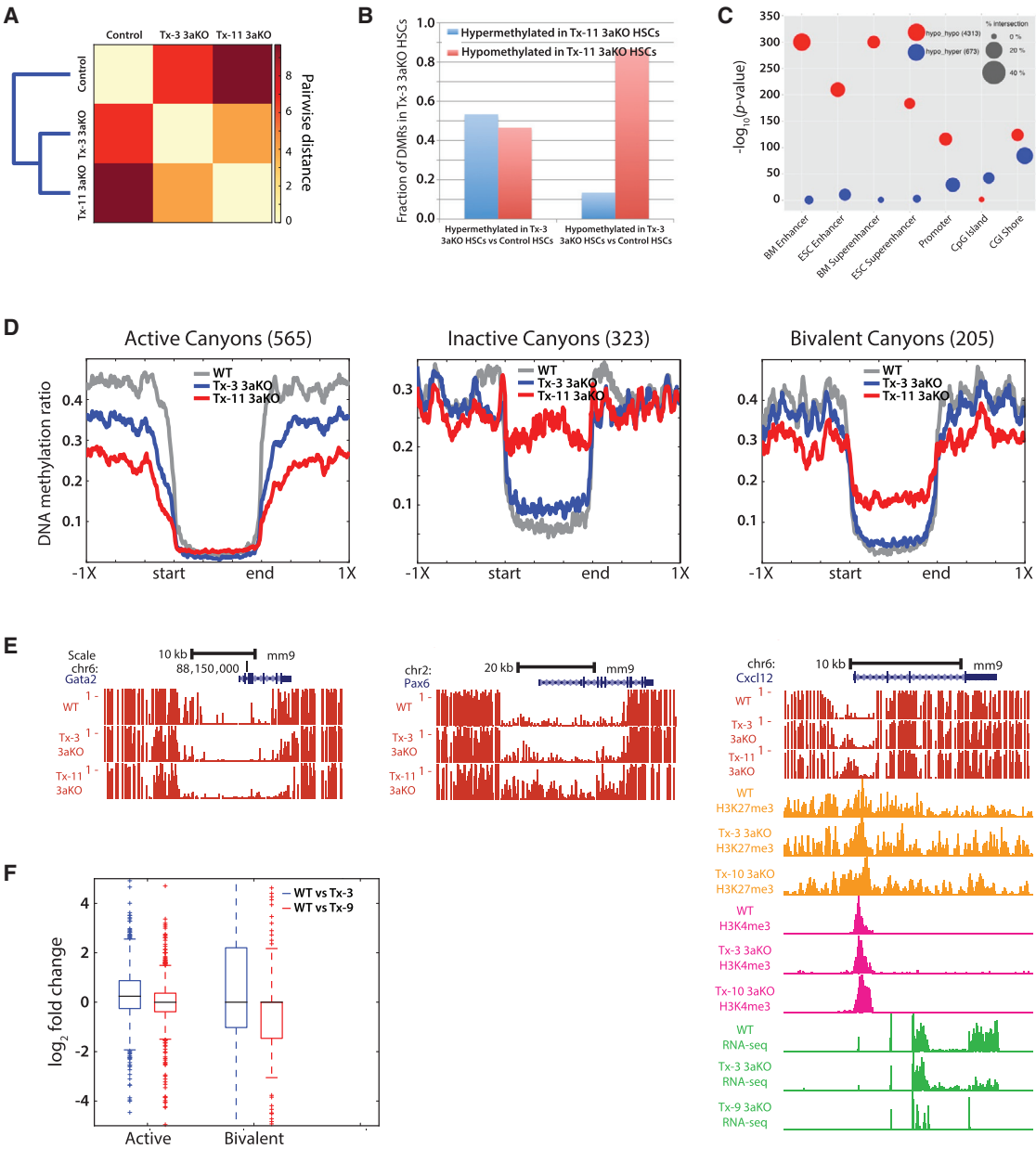

Figure 2. Dnmt3a Controls DNA Methylation at HSC Regulatory Elements

(A) Hierarchical clustering on the basis of CpG methylation ratio of control, Tx-3, and Tx-11 *Dnmt3a*^{KO} HSCs.

(B) Fraction of hyper- or hypo-methylated DMRs in Tx-3 *Dnmt3a*^{KO} HSCs (versus control HSCs) that became further hyper- or hypo-methylated in Tx-11 *Dnmt3a*^{KO} HSCs (versus Tx-3 *Dnmt3a*^{KO} HSCs).

(C) Enrichment analysis of 4,313 "hypo_hypo" regions compared with 673 control regions ("hypo_hyper"). Size of data points represents the overlap percentage with the size of the corresponding regulatory regions in the denominator.

(D) DNA methylation levels of active, bivalent, and inactive canyons in control (WT), Tx-3 *Dnmt3a*^{KO}, and Tx-11 *Dnmt3a*^{KO} HSCs. Flanking regions are extended by the same length as the corresponding canyon (±1×).

(E) DNA methylation profile of active, inactive, and bivalent canyon loci by WGBS. The height of each bar represents the DNA methylation level of an individual CpG. Also shown for *Cxcl12* are histone marks defining bivalent canyons and RNA-seq expression.

(F) Expression level changes of genes within active and bivalent canyon regions.

See also Figure S2.

exceptions include several imprinted genes (Figure S2G) such as *Ndn*, *Gtl2*, and *Peg3* implicated in stem cell function (Kubota et al., 2009; Qian et al., 2016; Berg et al., 2011). In summary, lack of *Dnmt3a* over serial passage stabilizes the self-renewing epigenome and leads to an inability to silence genes associated with maintenance of HSC identity.

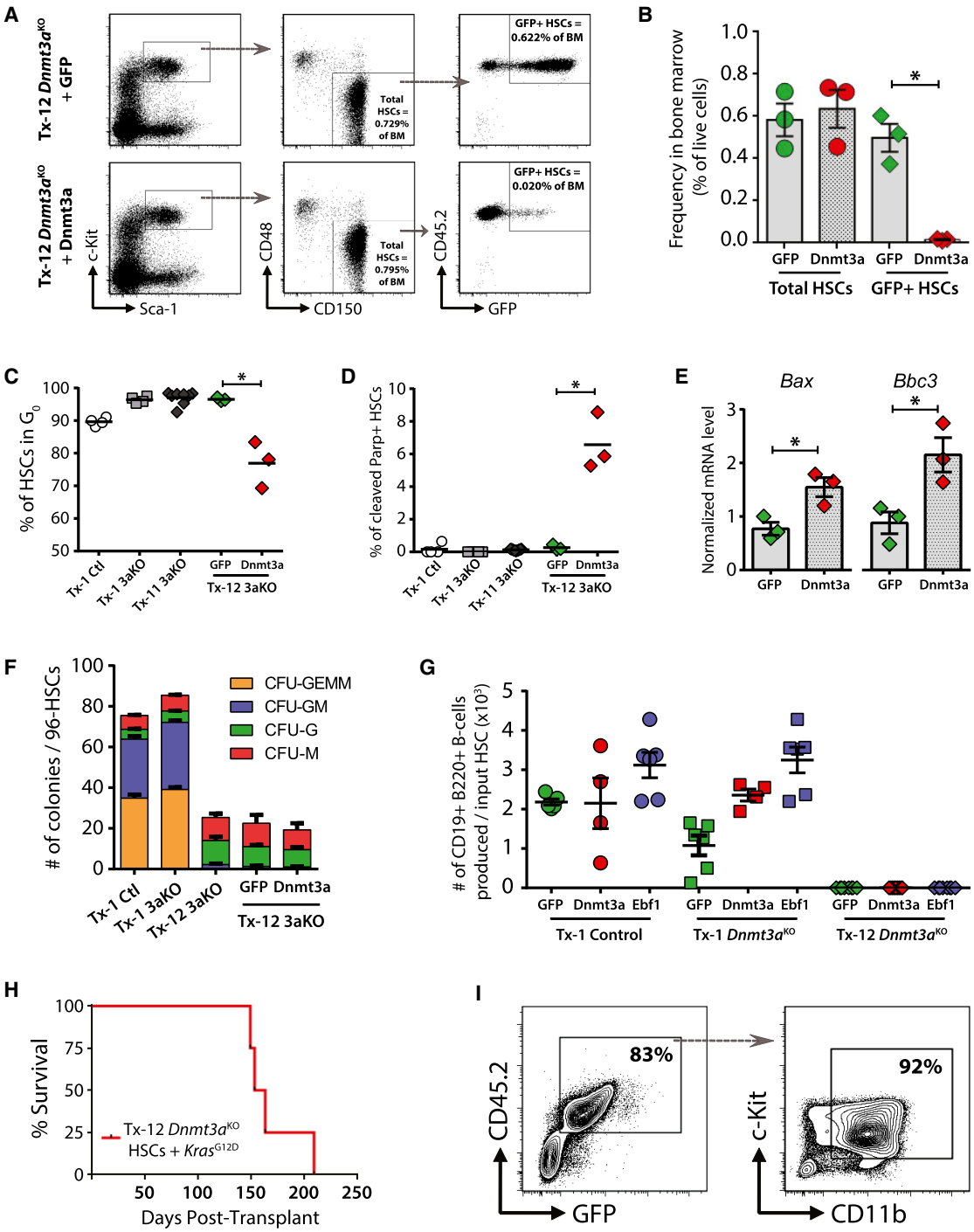

Figure 3. Differentiation Capacity Is Lost but Transformation Potential Is Retained in Immortalized *Dnmt3a*^{KO} HSCs

(A) Representative flow cytometry plots showing bone marrow analysis of mice transplanted with Tx-11 *Dnmt3a*^{KO} HSCs transduced with control (GFP) or *Dnmt3a*-expressing (Dnmt3a) lentivirus 18 weeks post-transplant.

(B) Frequency of transduced Tx-11 *Dnmt3a*^{KO} HSCs in bone marrow of recipient mice 18 weeks post-transplant.

(C) Cell cycle analysis of the indicated genotype/transplant stage showing proportion of quiescent (G_0) HSCs.

(D) Quantification of apoptotic HSCs of the indicated genotype/transplant stage.

(E) Expression of pro-apoptotic genes in Tx-11 *Dnmt3a*^{KO} HSCs transduced with control (GFP) or *Dnmt3a*-expressing (Dnmt3a) lentivirus.

(F) Clonogenic myeloid potential of HSCs from the indicated genotype/transplant stage.

(legend continued on next page)

Differentiation Capacity Is Lost but Transformation Potential Is Retained in Immortalized *Dnmt3a*^{KO} HSCs

We rescued late-passage *Dnmt3a*^{KO} HSCs with enforced expression of *Dnmt3a* to determine if differentiation capacity could be restored. Tx-11 *Dnmt3a*^{KO} HSCs were transduced with a lentivirus expressing full-length *Dnmt3a* (with bicistronic GFP) and transplanted. Re-expression of *Dnmt3a* led to the emergence of GFP^{+} cells in the peripheral blood at 4 weeks post-transplant (Figures S3A and S3B), which was not observed from transduction of the same HSCs with the control lentivirus. But ultimately, this initial output was not sustained (Figure S3C). However, ectopic expression of *Dnmt3a* did abrogate clonal expansion of the mutant HSCs in the bone marrow (Figure 3A). Although the total HSC frequency was identical in recipients of *Dnmt3a*^{KO} HSCs transduced with control or *Dnmt3a*-expressing lentivirus, GFP^{+} HSCs were severely depleted when expression of *Dnmt3a* was restored (Figure 3B). Re-expression of *Dnmt3a* induced proliferation (Figures 3C and S3D) and increased apoptosis (Figures 3D and S3E), which was associated with upregulation of the pro-apoptotic genes *Bbc3* (*puma*) and *Bax* (Figure 3E).

To evaluate differentiation capacity without cellular competition, myeloid potential of GFP^{+} *Dnmt3a*^{KO} HSCs was quantified by colony-forming assay. Myeloid potential of Tx-12 *Dnmt3a*^{KO} HSCs was severely compromised, and their differentiation was not rescued by complementation with *Dnmt3a*-expressing lentivirus (Figure 3F). Moreover, the colonies that were produced by late-passage *Dnmt3a*^{KO} HSCs were predominantly uni-lineage (Figure 3F). Similarly, re-expression of *Dnmt3a* was not able to restore T cell potential on OP9-DL1 co-culture (Schmitt and Zúñiga-Pflücker, 2002). Although *Dnmt3a* expression increased CD4^{+} T cell production, this output was marginal compared with control and early-passage *Dnmt3a*^{KO} HSCs (Figure S3F). But analysis of the double-negative (DN; CD4^{-} CD8a^{-}) population did show development through the early stages of T cell maturation. In fact, re-expression of *Dnmt3a* generated an abnormal CD25^{bright} DN2 cell population (Figure S3G), consistent with our observation that *Dnmt3a* is necessary for developmental progression of T cell progenitors (Kramer et al., 2017).

We then considered whether differentiation could bypass Dnmt3a. *Ebf1* is a master regulator of B cell potential (Lin and Grosschedl, 1995) located in a canyon that becomes hypermethylated with extended passage of *Dnmt3a*^{KO} HSCs. Tx-12 *Dnmt3a*^{KO} HSCs were transduced with control, *Dnmt3a*-expressing, or *Ebf1*-expressing lentivirus and co-cultured on OP9 stromal cells for 14 days. The B cell (B220^{+} CD19^{+}) differentiation deficit in early-passage *Dnmt3a*^{KO} HSCs was restored by expression of *Dnmt3a*, and like control HSCs, B cell output of early-passage *Dnmt3a*^{KO} HSCs was enhanced by overexpression of *Ebf1* (Figure 3G). In contrast, overexpression of neither *Dnmt3a* nor *Ebf1* was able to restore any B cell potential to late-passage *Dnmt3a*^{KO} HSCs (Figure 3G).

If differentiation potential was completely silenced, perhaps immortalized *Dnmt3a*^{KO} HSCs would be incapable of malignant transformation, given that some differentiation is required for generation of acute myeloid leukemia (AML) (Ye et al., 2015). Tx-12 *Dnmt3a*^{KO} HSCs were transduced with a lentivirus expressing *Kras*^{G12D}, a common mutation co-occurring with *DNMT3A* mutations in AML (Ley et al., 2013), and transplanted. Once GFP^{+} cells began emerging in the blood, mice rapidly succumbed (Figure 3H) to a fully penetrant AML with a c-Kit^{+} CD11b^{+} phenotype (Figure 3I). Thus, although differentiation was irreversibly blocked in immortalized *Dnmt3a*^{KO} HSCs, they retained the potential for malignant transformation when presented with an appropriate co-operating mutation.

Molecular Analysis of Dnmt3a Rescue, Dominant-Negative Mutant, and Clonal Hematopoiesis

DNA methylation was compared between Tx-12 *Dnmt3a*^{KO} HSCs transduced with either control or *Dnmt3a*-expressing lentivirus. Of 361 genomic regions hypomethylated in Tx-11 *Dnmt3a*^{KO} HSCs versus Tx-3 *Dnmt3a*^{KO} HSCs, 280 (77.6%) became hypermethylated in Tx-12 *Dnmt3a*^{KO} HSCs following re-expression of *Dnmt3a*, indicating that DNA methylation was re-established at the correct regions, including canyon boundaries (Figure 4A) and enhancers (Figure 4B). The re-establishment of DNA methylation patterns did not necessarily correlate with corresponding gene expression differences (Figure S4A), but perhaps this would normalized with further re-expression of *Dnmt3a* (Figure S4B).

We also compared the DNA methylation changes in *Dnmt3a*^{KO} HSCs with those in the context of mutations in patients. The most prevalent *DNMT3A* mutation is a missense at amino acid 882 (Ley et al., 2010). This mutation creates a dominant-negative protein with reduced DNA methyltransferase capacity (Russler-Germain et al., 2014; Kim et al., 2013). Global DNA methylation was performed on Tx-3 *Dnmt3a*$^{R878H/+}$ HSCs (*Dnmt3a*^{R878}; mouse homolog of human *DNMT3A*^{R882H}) (Guryanova et al., 2016) and compared with Tx-3 *Dnmt3a*^{KO} HSCs. Tx-3 *Dnmt3a*^{R878} HSCs displayed a self-renewal advantage over control HSCs, but not to the same degree as *Dnmt3a*^{KO} HSCs (Figure S4C). On a global scale, *Dnmt3a*^{R878} showed hypomethylation throughout the genome, although not to the same degree as *Dnmt3a*^{KO} HSCs (Figure 4C). There was high correlation between the regions affected by changes in DNA methylation in *Dnmt3a*^{R878} and *Dnmt3a*^{KO} HSCs. Of the DMRs shared between *Dnmt3a*^{R878} and *Dnmt3a*^{KO} HSCs compared with WT, 95.0% (1,653 of 1,730) showed hypermethylation in both mutant genotypes, while 95.6% (6,742 of 7,032) underwent hypomethylation in both mutant HSC genotypes. Of the 12,644 hypo-DMRs in *Dnmt3a*^{R878} HSCs compared with WT, 6,724 (53.2%) are hypo-DMRs in *Dnmt3a*^{KO} HSCs at the exact same genomic co-ordinates, with this fraction increasing if the genome windows are extended. Although overall methylation patterns were

(G) B cell potential of HSCs from the indicated genotype/transplant stage transduced with control (GFP), *Dnmt3a*-expressing, or *Ebf1*-expressing lentivirus.
(H) Time to morbidity in mice transplanted with Tx-12 *Dnmt3a*^{KO} HSCs transduced with lentivirus expressing *Kras*^{G12D}.
(I) Phenotype of *Kras*^{G12D}-driven AML.
Mean ± SEM values are shown. *$p < 0.05$, **$p < 0.01$. See also Figure S3.

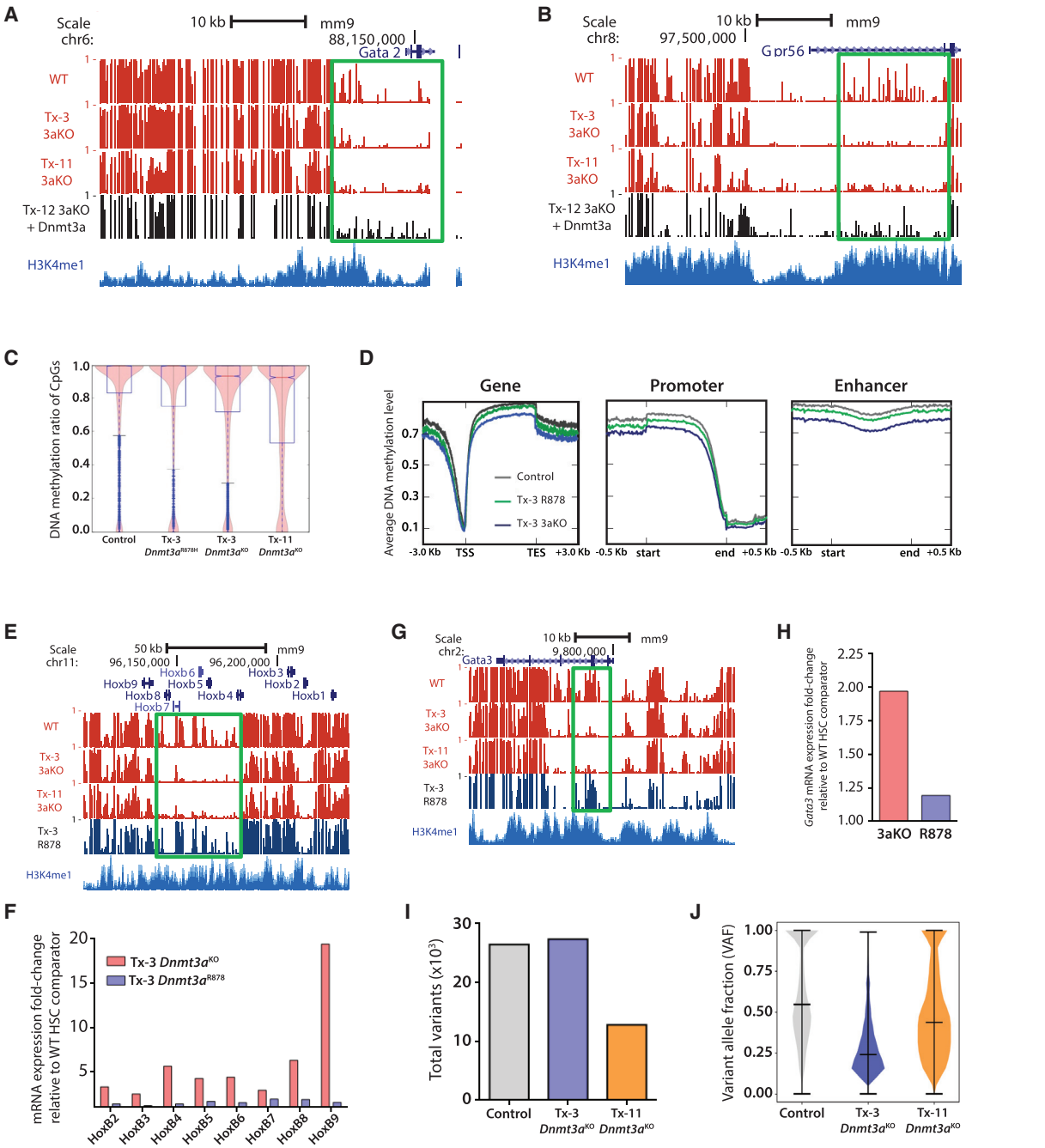

Figure 4. Molecular Analysis of Dnmt3a Rescue, Dominant-Negative Mutant, and Clonal Hematopoiesis

(A and B) WGBS profiles showing increased DNA methylation (green boxes) in *Gata2* canyon (A) and *Gpr56* enhancer (B) in Tx-11 *Dnmt3a*^{KO} HSCs transduced with *Dnmt3a*-expressing lentivirus.

(C) DNA methylation ratio of CpGs throughout the genome in HSCs of the indicated genotypes.

(D) Methylation levels of CpGs within gene bodies, promoters, and enhancers.

(E) DNA methylation profiles of the *HoxB* locus. Green box shows hypomethylation in *Dnmt3a*^{KO}, which is not observed in *Dnmt3a*^{R878} HSCs.

(F) Expression levels of *HoxB* genes in Tx-3 *Dnmt3a*^{KO} and Tx-3 *Dnmt3a*^{R878} HSCs. Data are expressed as relative fold change to control comparators in each sequencing experiment (n = 2–4 biological replicates per genotype).

(G and H) DNA methylation profile of *Gata3* locus showing hypomethylation of *Dnmt3a*^{KO} (3aKO) HSCs (green box) (G), corresponding with increased gene expression (H), not conserved in *Dnmt3a*^{R878} (R878) HSCs. Expression data are expressed as relative fold change to control comparators in each sequencing experiment (n = 2–4 biological replicates per genotype).

(I and J) Total number of somatic variants (I) and variant allele fraction (J) in HSCs from the indicated genotype/transplant stage.

See also Figure S4.

highly overlapping between the *Dnmt3a* mutant HSCs, there were distinct focal changes. For example, *Dnmt3a*^{R878} HSCs did not exhibit the hypermethylation of enhancer elements of differentiation factors such as *Pax5* and *Bcl11b* (Figure S4D). Similarly, the *HoxB* gene cluster, which becomes significantly hypomethylated in *Dnmt3a*^{KO} HSCs, did not show the same loss of DNA methylation in *Dnmt3a*^{R878} HSCs (Figure 4E) and corresponding transcriptional upregulation (Figure 4F). A CpG island in the *Gata3* promoter is particularly sensitive to *Dnmt3a* loss of function (Challen et al., 2011), but DNA methylation remained intact for this region in *Dnmt3a*^{R878} HSCs (Figure 4G), and gene expression was unchanged (Figure 4H). These findings suggest that *Dnmt3a*^{KO} and *Dnmt3a*^{R878H} mutations in HSCs result in similar overall DNA methylation changes, but methylation differences at specific stem cell enhancer elements may be important for the differentiation defects in the loss-of-function model.

The expansion of *Dnmt3a*^{KO} HSCs over extended passage was reminiscent of human CHIP, which can persist in a benign state for decades. To determine if this HSC expansion was associated with acquisition of co-operating mutations, exome sequencing was performed. The overall number of somatic variants was reduced in Tx-12 *Dnmt3a*^{KO} HSCs compared with early-passage HSCs (Figure 4I), but the variant allele fraction (VAF) of these variants was higher (Figure 4J), indicating the transplanted HSC pool was becoming more homogeneous over time. A reduced number of variants is consistent with reduced clonal complexity, while an increase in the VAF of individual variants (Tx-3 *Dnmt3a*^{KO} HSCs = 0.2400, Tx-12 *Dnmt3a*^{KO} HSCs = 0.4381) is consistent with heterozygous polymorphisms originating from dominant clones. However, analysis of the high-confidence somatic variants did not identify any acquired mutations which have been associated with human CHIP (Table S4).

As Dnmt3a has been suggested to regulate telomeres (Gonzalo et al., 2006) and telomere shortening limits HSC transplantability (Allsopp et al., 2003), we computationally predicted telomere length (Ding et al., 2014). Tx-12 *Dnmt3a*^{KO} HSCs showed no erosion of telomere length (Figure S4E; Table S4). Cumulatively, these data suggest *Dnmt3a* loss of function is sufficient to bias HSC fate decisions and initiate the pre-malignant condition of CHIP but is not sufficient to drive malignant transformation.

DISCUSSION

Here we show that loss of *Dnmt3a* endows HSCs with immortality *in vivo*. The self-renewal potential of *Dnmt3a*^{KO} HSCs far exceeds that of normal HSCs and the lifespan of the mice from which they were derived. Our data establish that HSCs do not have an inherently finite lifespan but that loss of *Dnmt3a* augments epigenetic features that enforce self-renewal and enable HSCs to be propagated indefinitely. Further examination of the mechanisms perpetuating immortality in *Dnmt3a*^{KO} HSCs may provide a window for artificially extending the lifespan of HSCs, an important biomedical application in the context of the aging human population.

The differentiation block of immortal *Dnmt3a*^{KO} HSCs cannot be rescued by re-expression of *Dnmt3a* or transcription factors such as *Ebf1*. But re-expression of *Dnmt3a* abrogated the self-renewal phenotype, suggesting the roles of Dnmt3a in self-renewal and differentiation can be uncoupled. Our data also demonstrate that malignant transformation is agnostic to DNA methylation state: both early-passage (Mayle et al., 2015; Celik et al., 2015) and late-passage (this study) *Dnmt3a*^{KO} HSCs will generate malignancies when an appropriate co-operating mutation is acquired. How oncogenic signals can overcome the differentiation block of *Dnmt3a*^{KO} HSCs to generate disease warrants further investigation.

Although we use an artificial system of serial transplantation, we consider the extent to which these insights may be extrapolated to humans. *DNMT3A* mutations are the most common mutation in CHIP (Xie et al., 2014; Jaiswal et al., 2014; Genovese et al., 2014), with increasing frequency with age (McKerrell et al., 2015; Young et al., 2016). But as CHIP is identified by assaying peripheral blood, if *DNMT3A* mutant human HSCs also show compromised differentiation, we predict the proportion of mutant HSCs in the bone marrow is underestimated by current studies. Our experiments are also distinct from the human scenario in that each transplant of *Dnmt3a*^{KO} HSCs contains fresh WT bone marrow replete with normal HSCs. In the aging human, WT HSCs diminish in function (Pang et al., 2011), offering less competition to emerging *DNMT3A* mutant clones. Even partial loss of *DNMT3A* function through weak heterozygous mutations, likely enables mutant HSCs to outcompete WT counterparts. We also show that a dominant-negative *Dnmt3a* mutation (R878) equivalent to the frequent human R882 mutation results in very similar DNA methylation changes to the null allele, suggesting most *DNMT3A* mutations likely produce similar molecular and cellular consequences at least at the level of clonal expansion.

The phenotype of *Dnmt3a*^{KO} HSCs is unique. Mutation of some other genes can enhance HSCs capacity (Rossi et al., 2012), but none can remove the inherent limits on self-renewal and replicative lifespan like *Dnmt3a*. Our data add to the emerging view that HSCs are in constant competition with their siblings. Perturbations that confer an advantage to one HSC over another will be selected depending on the specific context. With the enormous self-renewal capacity of *Dnmt3a*-null HSCs demonstrated here, a single mutant HSC in human bone marrow can outcompete WT counterparts over a period of many years, even if initially vastly outnumbered.

EXPERIMENTAL PROCEDURES

Further details and an outline of resources used in this work can be found in Supplemental Experimental Procedures.

Mice and Transplantation

All animal procedures were approved by Institutional Animal Care and Use Committees and performed in strict adherence to Washington University institutional guidelines. All mice were C57BL/6 background. Recipient CD45.1 mice (8–10 weeks of age; strain #002014; The Jackson Laboratory) were given a split dose of 10.5 Gy irradiation. Mx1-Cre(+):*Dnmt3a*$^{fl/fl}$ mice have been previously described by our group (Challen et al., 2011). Control mice were Mx1-Cre(+):*Dnmt3a*$^{+/+}$ mice. Deletion of floxed alleles was induced by intraperitoneal injection of 300 μg pIpC (#p1530; Sigma-Aldrich) six times every other day in adult mice (10–12 weeks old). Equal numbers of male and female mice were used.

For competitive transplants, 200 HSCs (Lineage$^-$ [Gr-1, Mac-1, B220, CD3e, Ter119], c-Kit$^+$, Sca-1$^+$, CD48$^-$, CD150$^+$) were transplanted with 2.5 × 10^5 WT CD45.1 competitor bone marrow. For serial transplantation, 200 donor-derived HSCs were isolated from the previous recipients 18–24 weeks post-transplant

and transplanted into new lethally irradiated recipients along with fresh WT competitor bone marrow. Recipients were bled through the retro-orbital route and analyzed for donor-derived lineage contribution by flow cytometry.

Quantification and Statistical Analysis

Statistical comparisons between groups were evaluated using Student's t test or ANOVA as appropriate using Prism 6 (GraphPad). All data are presented as mean ± SE. Time to morbidity is presented in Kaplan-Meier survival curves and analyzed using the log-rank test. Statistical significance is denoted as $*p < 0.05$, $**p < 0.01$, and $***p < 0.001$; n indicates the number of biological replicates within each group.

DATA AND SOFTWARE AVAILABILITY

The accession number for the raw and processed whole-genome bisulfite sequencing (WGBS), histone modification, and RNA sequencing data reported in this paper is GEO: GSE98191. UCSC Genome Browser tracks (mouse mm9) can be accessed from the hub http://lilab.research.bcm.edu/dldcc-web/lilab/hjpark/multipleTransplants/hub.txt. The accession number for the exome sequencing data reported in this paper is SRA: SRP133364.

SUPPLEMENTAL INFORMATION

Supplemental Information includes Supplemental Experimental Procedures, four figures, and four tables and can be found with this article online at https://doi.org/10.1016/j.celrep.2018.03.025.

ACKNOWLEDGMENTS

We thank the Siteman Cancer Center (Washington University, Core Grant CA91842) and the Dan L. Duncan Cancer Center (Baylor College of Medicine, Core Grant CA125123). This work was supported by NIH grants DK102428 (to G.A.C.), HG007538 and CA193466 (to W.L.), HL132074 (to L.D.), CA178191 (to O.A.G.), and DK092883, CA183252 and AG036695, and CPRIT RP140053 (to M.A.G.). M.J. was supported by grant 5T32DK60445. H.C. was supported by an American Society of Hematology scholar award. E.L.O. was supported by NIH grant 5T32CA113275. Y.L. is supported by a NYSTEM training grant. J.M.R. was supported by grant GM056929.

AUTHOR CONTRIBUTIONS

Conceptualization, G.A.C.; Methodology, M.J., H.J.P., H.C., Y. Lee, W.L., M.A.G., and G.A.C.; Software, H.J.P., J.M.R., B.R., and W.L.; Validation, M.J., H.J.P., M.A.G., and G.A.C.; Formal Analysis, M.J., H.J.P., J.M.R., B.R., M.A.G., and G.A.C.; Investigation, M.J., H.C., E.L.O., A.G., Y. Lei, and G.A.C.; Resources, L.D., O.A.G., W.L., M.A.G., and G.A.C.; Data Curation, H.J.P., W.L., M.A.G., and G.A.C.; Writing – Original Draft Preparation, M.J., H.J.P., H.C., and G.A.C.; Writing – Review & Editing, M.A.G. and G.A.C.; Visualization, M.J., H.J.P., H.C., E.L.O., M.A.G., and G.A.C.; Supervision, M.A.G. and G.A.C.; Project Administration, M.A.G. and G.A.C.; Funding Acquisition, M.A.G. and G.A.C.

DECLARATION OF INTERESTS

The authors declare no competing interests.

Received: May 11, 2017
Revised: January 19, 2018
Accepted: March 7, 2018
Published: April 3, 2018

REFERENCES

Allsopp, R.C., Morin, G.B., DePinho, R., Harley, C.B., and Weissman, I.L. (2003). Telomerase is required to slow telomere shortening and extend replicative lifespan of HSCs during serial transplantation. Blood *102*, 517–520.

Berg, J.S., Lin, K.K., Sonnet, C., Boles, N.C., Weksberg, D.C., Nguyen, H., Holt, L.J., Rickwood, D., Daly, R.J., and Goodell, M.A. (2011). Imprinted genes that regulate early mammalian growth are coexpressed in somatic stem cells. PLoS ONE *6*, e26410.

Celik, H., Mallaney, C., Kothari, A., Ostrander, E.L., Eultgen, E., Martens, A., Miller, C.A., Hundal, J., Klco, J.M., and Challen, G.A. (2015). Enforced differentiation of Dnmt3a-null bone marrow leads to failure with c-Kit mutations driving leukemic transformation. Blood *125*, 619–628.

Challen, G.A., Sun, D., Jeong, M., Luo, M., Jelinek, J., Berg, J.S., Bock, C., Vasanthakumar, A., Gu, H., Xi, Y., et al. (2011). Dnmt3a is essential for hematopoietic stem cell differentiation. Nat. Genet. *44*, 23–31.

Challen, G.A., Sun, D., Mayle, A., Jeong, M., Luo, M., Rodriguez, B., Mallaney, C., Celik, H., Yang, L., Xia, Z., et al. (2014). Dnmt3a and Dnmt3b have overlapping and distinct functions in hematopoietic stem cells. Cell Stem Cell *15*, 350–364.

Chambers, S.M., Boles, N.C., Lin, K.Y., Tierney, M.P., Bowman, T.V., Bradfute, S.B., Chen, A.J., Merchant, A.A., Sirin, O., Weksberg, D.C., et al. (2007). Hematopoietic fingerprints: an expression database of stem cells and their progeny. Cell Stem Cell *1*, 578–591.

Corces-Zimmerman, M.R., Hong, W.J., Weissman, I.L., Medeiros, B.C., and Majeti, R. (2014). Preleukemic mutations in human acute myeloid leukemia affect epigenetic regulators and persist in remission. Proc. Natl. Acad. Sci. U S A *111*, 2548–2553.

Ding, Z., Mangino, M., Aviv, A., Spector, T., Durbin, R., and Consortium, U.K.; UK10K Consortium (2014). Estimating telomere length from whole genome sequence data. Nucleic Acids Res. *42*, e75.

Genovese, G., Kähler, A.K., Handsaker, R.E., Lindberg, J., Rose, S.A., Bakhoum, S.F., Chambert, K., Mick, E., Neale, B.M., Fromer, M., et al. (2014). Clonal hematopoiesis and blood-cancer risk inferred from blood DNA sequence. N. Engl. J. Med. *371*, 2477–2487.

Gonzalo, S., Jaco, I., Fraga, M.F., Chen, T., Li, E., Esteller, M., and Blasco, M.A. (2006). DNA methyltransferases control telomere length and telomere recombination in mammalian cells. Nat. Cell Biol. *8*, 416–424.

Guryanova, O.A., Shank, K., Spitzer, B., Luciani, L., Koche, R.P., Garrett-Bakelman, F.E., Ganzel, C., Durham, B.H., Mohanty, A., Hoermann, G., et al. (2016). DNMT3A mutations promote anthracycline resistance in acute myeloid leukemia via impaired nucleosome remodeling. Nat. Med. *22*, 1488–1495.

Harrison, D.E., and Astle, C.M. (1982). Loss of stem cell repopulating ability upon transplantation. Effects of donor age, cell number, and transplantation procedure. J. Exp. Med. *156*, 1767–1779.

Jaiswal, S., Fontanillas, P., Flannick, J., Manning, A., Grauman, P.V., Mar, B.G., Lindsley, R.C., Mermel, C.H., Burtt, N., Chavez, A., et al. (2014). Age-related clonal hematopoiesis associated with adverse outcomes. N. Engl. J. Med. *371*, 2488–2498.

Jeong, M., Sun, D., Luo, M., Huang, Y., Challen, G.A., Rodriguez, B., Zhang, X., Chavez, L., Wang, H., Hannah, R., et al. (2014). Large conserved domains of low DNA methylation maintained by Dnmt3a. Nat. Genet. *46*, 17–23.

Kim, S.J., Zhao, H., Hardikar, S., Singh, A.K., Goodell, M.A., and Chen, T. (2013). A DNMT3A mutation common in AML exhibits dominant-negative effects in murine ES cells. Blood *122*, 4086–4089.

Kramer, A.C., Kothari, A., Wilson, W.C., Celik, H., Nikitas, J., Mallaney, C., Ostrander, E.L., Eultgen, E., Martens, A., Valentine, M.C., et al. (2017). Dnmt3a regulates T-cell development and suppresses T-ALL transformation. Leukemia *31*, 2479–2490.

Kubota, Y., Osawa, M., Jakt, L.M., Yoshikawa, K., and Nishikawa, S. (2009). Necdin restricts proliferation of hematopoietic stem cells during hematopoietic regeneration. Blood *114*, 4383–4392.

Ley, T.J., Ding, L., Walter, M.J., McLellan, M.D., Lamprecht, T., Larson, D.E., Kandoth, C., Payton, J.E., Baty, J., Welch, J., et al. (2010). DNMT3A mutations in acute myeloid leukemia. N. Engl. J. Med. *363*, 2424–2433.

Ley, T.J., Miller, C., Ding, L., Raphael, B.J., Mungall, A.J., Robertson, A., Hoadley, K., Triche, T.J., Jr., Laird, P.W., Baty, J.D., et al.; Cancer Genome Atlas

Research Network (2013). Genomic and epigenomic landscapes of adult de novo acute myeloid leukemia. N. Engl. J. Med. *368*, 2059–2074.

Lin, H., and Grosschedl, R. (1995). Failure of B-cell differentiation in mice lacking the transcription factor EBF. Nature *376*, 263–267.

Mayle, A., Yang, L., Rodriguez, B., Zhou, T., Chang, E., Curry, C.V., Challen, G.A., Li, W., Wheeler, D., Rebel, V.I., and Goodell, M.A. (2015). Dnmt3a loss predisposes murine hematopoietic stem cells to malignant transformation. Blood *125*, 629–638.

McKerrell, T., Park, N., Moreno, T., Grove, C.S., Ponstingl, H., Stephens, J., Crawley, C., Craig, J., Scott, M.A., Hodkinson, C., et al.; Understanding Society Scientific Group (2015). Leukemia-associated somatic mutations drive distinct patterns of age-related clonal hemopoiesis. Cell Rep. *10*, 1239–1245.

Micklem, H.S., Lennon, J.E., Ansell, J.D., and Gray, R.A. (1987). Numbers and dispersion of repopulating hematopoietic cell clones in radiation chimeras as functions of injected cell dose. Exp. Hematol. *15*, 251–257.

Pang, W.W., Price, E.A., Sahoo, D., Beerman, I., Maloney, W.J., Rossi, D.J., Schrier, S.L., and Weissman, I.L. (2011). Human bone marrow hematopoietic stem cells are increased in frequency and myeloid-biased with age. Proc. Natl. Acad. Sci. U S A *108*, 20012–20017.

Pløen, G.G., Nederby, L., Guldberg, P., Hansen, M., Ebbesen, L.H., Jensen, U.B., Hokland, P., and Aggerholm, A. (2014). Persistence of DNMT3A mutations at long-term remission in adult patients with AML. Br. J. Haematol. *167*, 478–486.

Qian, P., He, X.C., Paulson, A., Li, Z., Tao, F., Perry, J.M., Guo, F., Zhao, M., Zhi, L., Venkatraman, A., et al. (2016). The Dlk1-Gtl2 locus preserves LT-HSC function by inhibiting the PI3K-mTOR pathway to restrict mitochondrial metabolism. Cell Stem Cell *18*, 214–228.

Rossi, L., Lin, K.K., Boles, N.C., Yang, L., King, K.Y., Jeong, M., Mayle, A., and Goodell, M.A. (2012). Less is more: unveiling the functional core of hematopoietic stem cells through knockout mice. Cell Stem Cell *11*, 302–317.

Russler-Germain, D.A., Spencer, D.H., Young, M.A., Lamprecht, T.L., Miller, C.A., Fulton, R., Meyer, M.R., Erdmann-Gilmore, P., Townsend, R.R., Wilson, R.K., and Ley, T.J. (2014). The R882H DNMT3A mutation associated with AML dominantly inhibits wild-type DNMT3A by blocking its ability to form active tetramers. Cancer Cell *25*, 442–454.

Schmitt, T.M., and Zúñiga-Pflücker, J.C. (2002). Induction of T cell development from hematopoietic progenitor cells by delta-like-1 in vitro. Immunity *17*, 749–756.

Shlush, L.I., Zandi, S., Mitchell, A., Chen, W.C., Brandwein, J.M., Gupta, V., Kennedy, J.A., Schimmer, A.D., Schuh, A.C., Yee, K.W., et al.; HALT Pan-Leukemia Gene Panel Consortium (2014). Identification of pre-leukaemic haematopoietic stem cells in acute leukaemia. Nature *506*, 328–333.

Siminovitch, L., Till, J.E., and McCulloch, E.A. (1964). Decline in colony forming ability of marrow cells subjected to serial transplantation into Irradiated mice. J. Cell. Comp. Physiol. *64*, 23–31.

Spencer, D.H., Russler-Germain, D.A., Ketkar, S., Helton, N.M., Lamprecht, T.L., Fulton, R.S., Fronick, C.C., O'Laughlin, M., Heath, S.E., Shinawi, M., et al. (2017). CpG island hypermethylation mediated by DNMT3A is a consequence of AML progression. Cell *168*, 801–816.e13.

Xie, M., Lu, C., Wang, J., McLellan, M.D., Johnson, K.J., Wendl, M.C., McMichael, J.F., Schmidt, H.K., Yellapantula, V., Miller, C.A., et al. (2014). Age-related mutations associated with clonal hematopoietic expansion and malignancies. Nat. Med. *20*, 1472–1478.

Yang, L., Rau, R., and Goodell, M.A. (2015). DNMT3A in haematological malignancies. Nat. Rev. Cancer *15*, 152–165.

Ye, M., Zhang, H., Yang, H., Koche, R., Staber, P.B., Cusan, M., Levantini, E., Welner, R.S., Bach, C.S., Zhang, J., et al. (2015). Hematopoietic differentiation is required for initiation of acute myeloid leukemia. Cell Stem Cell *17*, 611–623.

Young, A.L., Challen, G.A., Birmann, B.M., and Druley, T.E. (2016). Clonal haematopoiesis harbouring AML-associated mutations is ubiquitous in healthy adults. Nat. Commun. *7*, 12484.

Cell Reports, Volume *23*

Supplemental Information

Loss of Dnmt3a Immortalizes Hematopoietic Stem Cells *In Vivo*

Mira Jeong, Hyun Jung Park, Hamza Celik, Elizabeth L. Ostrander, Jaime M. Reyes, Anna Guzman, Benjamin Rodriguez, Yong Lei, Yeojin Lee, Lei Ding, Olga A. Guryanova, Wei Li, Margaret A. Goodell, and Grant A. Challen

SUPPLEMENTAL EXPERIMENTAL PROCEDURES

Further information and requests for resources and reagents should be directed to and will be fulfilled by the Lead Contact, Grant A. Challen (gchallen@dom.wustl.edu).

Mice

All mice used in this study were C57Bl/6 background. Recipient mice for bone marrow transplants were originally purchased from The Jackson Laboratory (strain #002014) and maintained as a breeder colony under specific pathogen free (SPF) conditions. Recipient mice were typically 8-10 weeks of age at time of transplant. Mx1-Cre(+):*Dnmt3a*$^{fl/fl}$ mice have been previously described by our group. Control mice used in this study were Mx1-Cre(+):*Dnmt3a*$^{+/+}$ mice. Deletion of floxed alleles was induced by intraperitoneal injection of 300 µg pIpC (Sigma #p1530) six times every other day in adult mice (10-12 weeks old). Mice were allowed to recover for six weeks after the last injection, then confirmed for efficient floxed allele deletion by PCR genotyping pf peripheral blood neutrophils (Gr-1+ Mac-1+). Equal numbers of male and female mice were used in all studies.

Mice were monitored daily by laboratory staff and veterinary personnel for health and activity. Mice were given *ad libitum* access to water and standard mouse chow, with 12-hour light/dark cycles. Colonies were maintained in an SPF barrier facility, with quarterly testing of pathogens in sentinel animals housed in the same room. All laboratory staff wear personal protective clothing, and all manipulations were performed in biosafety cabinets in procedure rooms in the same animal suite. All animal procedures were approved by the Institutional Animal Care and Use Committee and performed in strict adherence to Washington University and Baylor College of Medicine institutional guidelines.

Bone Marrow Transplantation

For competitive transplants, 200 HSCs (Lineage- [Gr-1, Mac-1, B220, CD3e, Ter119], c-Kit+, Sca-1+, CD48-, CD150+) were transplanted into lethally irradiated recipients (following a split dose of 10.5 Gy total whole body irradiation four hours apart; Cesium-137 irradiator) along with $2.5x10^5$ wild-type whole bone marrow (WBM) by retro-orbital injection. In transplanted recipients, donor cells can be distinguished from wild-type competitor cells via CD45 allelic isoforms, where CD45.2 cells were donor- and CD45.1 were competitor-derived and matched to the recipient. For serial HSC transplantation, 200 donor-derived HSCs were isolated from the previous recipients 18-24 weeks post-transplant by FACS and transplanted into new lethally irradiated recipients along with fresh wild-type competitor WBM. This process was repeated for 12 successive rounds. Transplant recipients were bled through the retro-orbital route and analyzed for donor- and

competitor-derived lineage contribution in peripheral blood by flow cytometry. Peripheral blood counts were performed with a Hemavet 950 (Drew Scientific Group). Peripheral blood smears and bone marrow and spleen cytospins were stained with the Hema 3 stat pack (Fisher Scientific) and images were captured with a Nikon Microphot-SA microscope.

Cell Purification and Flow Cytometry

Peripheral blood was subject to red blood cell lysis and then stained using the following cell surface markers: Gr-1$^+$ and Mac-1$^+$ (Myeloid lineage), B220$^+$ (B-cell lineage), CD3e$^+$ (T-cell lineage) as well as CD45.2 and CD45.1 to discriminate donor versus competitor-derived peripheral blood contribution. For donor-derived HSC enumeration at the end of each transplant stage, bones were collected from individual mice (2 femurs, 2 tibias, 2 ileac crests) and used for a total viable cell count from the bone marrow. $7x10^6$ WBM cells per mouse were used for flow cytometric quantification of donor-derived HSC frequency. Total donor-derived HSC number was extrapolated by multiplying HSC frequency by total viable WBM per mouse. The following gating strategies were used to analyze or sort BM HSCs isolated from transplant-receiving mice: CD45.1-, CD45.2+, Lineage− [Gr1, Mac1, B220, CD3, Ter119], c-Kit+, Sca-1+, CD48-, CD150+. All antibody staining is performed in HBSS buffer (Corning #21021CV) containing Pen/Strep (100 Units/mL; Fisher Scientific #MT30002CI), HEPES (10uM; Life Technologies # 15630080) and FBS (2%; Sigma #14009C). Cells were suspended at a concentration of $1x10^8$ cells/mL and incubated on ice for 20 minutes with the desired antibodies listed in **Resource Table**. For competitive transplantations, magnetic enrichment was carried out using AutoMACS Pro Seperator (Miltenyi Biotec #130-092-545) with mouse anti-CD117 conjugated microbeads (Miltenyi Biotec #130-091-224). Post-enrichment, the positive cell fraction was stained with appropriate antibodies and sorted by FACS using antibodies described above from the enriched sample. Cell sorting and analysis was performed at the Siteman Cancer Center flow cytometry core and the Department of Pathology and Immunology flow cytometry core at Washington University School of Medicine.

Immunostaining of bone sections

Freshly dissected femurs were fixed in 4% PFA-based fixative at 4℃ for 3h. The bones were embedded in 8% gelatin in PBS. The tissues were snap frozen with liquid nitrogen and stored at -80℃ prior to sectioning. Bone sections were cut at 7μm using a CryoJane system (Instrumedics) and air dried overnight at room temperature. Sections were re-hydrated in PBS for 5 min and blocked using 5% goat serum in PBS for 30 min. Slides were incubated in rat-anti-

CD150 antibody (TC15-12F12.2; Biolegend) overnight at 4℃. CD150 was visualized by incubation in anti-rat Alexa Fluor 555 antibody (Thermo Fisher Scientific) for 2hr at room temperature with three washes in between. Rat IgG (Sigma Aldrich) was then applied to the slides for 10 min and washed with PBS. FITC-conjugated anti-B220, anti-Gr-1, anti-Mac1, anti-CD5, anti-CD8a, anti-CD2, anti-CD3e, anti-CD41, anti-Ter119 and anti-CD48 antibodies (eBioscience) along with rabbit-anti-laminin antibody (Sigma Aldrich) were used for subsequent primary staining at 4℃ overnight. Anti-FITC Alexa Fluor 488 (Jackson ImmunoResearch) and anti-rabbit Alexa Fluor 647 (Thermo Fisher Scientific) were used for secondary staining at room temperature for 2 hr. Slides were mounted with Prolong gold antifade (Invitrogen) and images were acquired on Nikon Ti Eclipse confocal microscopes.

Plasmids, Cloning and Viral Transduction

Mouse *Kras* cDNA was obtained from Origene (NM_021284). The G12D mutation was created using site-directed mutagenesis kit according to manufacturer's instructions (Agilent Technologies, #200522-5). Mouse *Dnmt3a* and *Ebf1* cDNAs were obtained from Open Biosystems (#BC007466) and Addgene (#96965) respectively. *Kras*^{G12D}, *Dnmt3a* and *Ebf1* cDNA were PCR amplified (see **Resource Table** for primer sequences) and cloned into the HIV-pMND-IRES-GFP lentiviral vector. For lentiviral production, 293T cells were co-transfected with the packaging plasmids pMD.G, psPAX2 and either pMND-IRES-GFP, pMND-*Dnmt3a*-IRES-GFP, pMND-*Kras*^{G12D}-IRES-GFP, or pMND-*Ebf1*-IRES-GFP using PEI-based transfection protocol (Polysciences # 23966-1). Transfections for lentivirus production were performed in 150 x 25 mm tissue culture dishes (Falcon # 353025) when 293T cells reached at least 80-90% of confluency. 48-hours post-transfection, 293T cell supernatants were collected and concentrated by centrifugation at 76,000g for 1.5 hours at 4°C.

For lentiviral transduction, target cells were adjusted to 2.5x10^5 cells/100uL in Stempro-34 medium (Gibco #10639011) supplemented with Pen-Strep (100 Units/mL), L-glutamine (2 mM), murine stem cell factor (100 ng/mL), murine thrombopoietin (100 ng/mL), murine Flt3L (50 ng/mL), murine interleukin-3 (5 ng/mL), and polybrene (4 mg/mL; Sigma), and spin-infected with the respective high-titer lentivirus preparations at 250g for 2 hours in a 96-well plate. 24 hours post-transduction, 1x10^5 transduced cells were transplanted into lethally irradiated mice by retro-orbital injection or used for *in vitro* assays.

Clonogenic Methocult Assay

Single HSCs (CD45.2+, Lineage−, c-Kit+, Sca-1+, CD48-, CD150+) were directly sorted into 96-well plates containing Methocult 3434 medium (Stem Cell Technologies #03434) and cultured *in vitro* at 37^{o}C for 14-days.

***in vitro* B-cell and T-cell differentiation assays**

For B-cell assay, 250 HSCs were sorted directly into wells of 24-well plates seeded with 5x10^{4} OP9 stromal cells. Cells were cultured for 14-days in the presence of recombinant mouse Flt3L (2.5 ng/mL; Miltenyi Biotec) and IL-7 (2.5 ng/mL; Miltenyi Biotec) with half media changes every fourth day. Following the culture period, cells were stained with B-cells markers (CD19, B220) and analyzed by flow cytometry.

For T-cell assay, 500 HSCs were sorted directly into wells of 24-well plates seeded with 5x10^{4} OP9-DL1 stromal cells (Schmitt and Zuniga-Pflucker, 2002). Cells were cultured for 28-days in the presence of recombinant mouse Flt3L and IL-7 with half media changes every fourth day. For days 0 to 16, Flt3L and IL-7 concentrations in the culture was 5ng/mL. For days 16 to 28, concentration of IL7 is reduced to 1 ng/mL to allow early T-cell progenitors (DN1 and DN2 stage cells) to progress through maturation. Following the 28-day culture period, cells were stained with T-cells markers and analyzed by flow cytometry. [DN1 (CD4-, CD8-, CD44+, CD25-), DN2 (CD4-, CD8-, CD44+, CD25+), DN3 (CD4-, CD8-, CD44-, CD25+), DN4 (CD4-, CD8-, CD44-, CD25-), CD4+ (CD4+, CD8-), CD8+ (CD4-, CD8+)].

Ki67/DAPI and Cleaved Parp staining

WBM from recipient mice was stained with HSC cell surface markers as described. For intracellular Ki67/DAPI (cell-cycle) or Cleaved Parp (apoptosis) staining, WBM cells were fixed and permeabilized using BD Cytofix/Cytoperm kit according to manufacturer's protocol (#554714) and stained with either an anti-Ki67-BV605 (BioLegend #652413) or anti-cleaved Parp-PE (BD Biosciences #552933) for 1h at room temperature. DAPI (Invitrogen #D3571) was added to cell samples containing anti-Ki67-BV605 and allowed to incubate for 20 min at RT before analysis.

Whole genome bisulfite sequencing

Genomic DNA was extracted from sorted HSCs using the PureLink Genomic DNA mini kit (Invitrogen #K182001). Bisultife conversion and purification was carried out using 100ng of genomic DNA and the EZ DNA Methylation Gold kit (Zymo Research #D5005). This process deaminates unmethylated cytosine risidues to uracil leaving methylated cytosine residues unchangesd. After bisulfite conversion, the Truseq DNA Methylation kit (Illumina, #EGMK81312)

was used for WGBS library preparation. Briefly, after bisulfite conversion, anneal the DNA synthesis primers to the converted and denatured ssDNA and synthesize DNA containing a specific sequence tag from the random hexamers and add terminal tagging oligo and synthesize complementary sequence. After making di-tagged DNA with known sequence tags at the 3' and 5' ends, clean-up tagged DNA using Ampure XP beads (Beckman Coulter # 5067-5582). Finally add Illumina single-index and amplify the library and using index primers and 10 cycles PCR program with 95°C for 30 seconds, 55°C for 30 seconds, 68°C for 3 minutes. Clean-up the PCR amplified final library using 1X Ampure XP beads and quantify library using KAPA library quantification kit (Kapa Biosystem #KK4844) and run 1 ul of undiluted library on the tape station using D1000 screen tape (Agilent #5056-5582). Paired-end 85bp sequencing was performed using Nextseq 500 mid output kit (FC-404-2001) with Illumina NextSeq platform. The data quality was checked with fastQC tool.

Paired-end sequencing reads from bisulfite-treated samples were aligned to the mm9 mouse genome. Adaptors and low-quality reads were trimmed using BSMAP with default settings. MOABS further selected only properly paired and uniquely mapped pairs for further analyses. Sequencing depth for CpGs with at least five reads for each sample was extracted to calculate the methylation ratio calling [0, 1] by the software MOABS (Sun et al., 2014). A two-state first-order hidden Markov model was used to detect hypomethylated regions and larger hypomethylated canyons (≥3.5 kb) as previously described (Jeong et al., 2013). To identify differentially methylated regions (DMRs) in pairwise comparisons, we developed a custom pipeline that extends the identified DMCs. DMCs were identified by pairwise comparison of WGBS profiles using the software MOABS with at least five differentially methylated CpG sites. We take sets of more than three DMCs in the same direction (hyper or hypo) within 300 bp as seed DMRs. The seed DMRs were then extended to include neighboring DMRs of the same direction if they are (1) within 300 bp and (2) not interrupted by a DMR of the other direction. To detect hypomethylated regions and larger hypomethylated canyons (≥3.5 kb), a two-state first-order hidden Markov model was used as previously described (Jeong et al., 2013). Mouse annotation information for RefSeq genes and CpG islands was downloaded from the UCSC Genome Browser. CpG island shores were defined as regions 0-2 kb away from CpG islands. Promoter regions were defined as regions 0-5kb upstream of RefSeq gene. Enhancers for mouse hematopoietic stem cell and bone marrow cell are defined from mouse Encode (Hon et al., 2013). Super enhancers are calculated based on H3K27ac data for the corresponding cell lines (Shen et al., 2012) by ROSE software (Lovén et al., 2013). Further, 300 sets of binding sites for 254 mouse transcription factors defined in 11 mouse cell types were downloaded from TFClass server (Wingender et al., 2013). Their enrichment to genomic regions of our interest (e.g. hypo_hypo) were computed using BEDtools (fisher

command)(Quinlan, 2014). Hierarchical clustering was based on euclidean distance among conditions. Enrichment analysis between sets of genomic regions was conucted by bedtools fisher command. Visualizing signal density (e.g. methylation ratio across genomic regions) was made by deepTools. Other visualization was made from matplotlib packages.

RNA-seq

RNA-seq was performed using the illumine Truseq Stranded mRNA library kit (Illumina #RS-122-2101). Total RNA was isolated from sorted HSCs using RNeasy micro kit (Qiagen #28006) together with RNase-free DNase treatment on the column (Qiagen #79254). RNA samples were poly-A selected and fragmented. First-strand and second-strand cDNA synthesized and followed by A-tailing and adaptor ligation. Ligated double strand libraries are purified and amplified 8-9 cycles. Multiplexed libraries were pooled and paired-end 100bp sequencing was performed on one flow-cell of an Illumina HiSeq 2500. Reads were mapped in TopHat 2.0.10. Differentially expressed genes were identified using Cufflinks 2.1.1 with relative fold-changes >2 in either direction.

ChIP-seq

Chromatin Immunoprecipitation (ChIP) was performed as described previously (Luo et al 2015). Briefly, Sorted HSCs were crossedlinked with 1% formaldehyde at room temperature for 10 min, and the reaction was stopped by 0.125M glycine at RT 5 min. Cross linked cells were washed once with ice cold PBS containing protease inhibitor cocktail (GenDepot #P3100-001) and the cell pellet was stored at -80°C. Cells were thawed on ice and lysed in 50µl lysis buffer (10 mM Tris pH 7.5, 1mM EDTA, 1% SDS), then diluted with 150 µl of PBS/PIC, and sonicated using Bioruptor (Diagenode) 30sec on 30 sec off 7 cycles to 200-500 bp fragments. The sonicated chromatin was centrifuged at 4°C for 5 min at 13,000rpm to remove precipitated SDS. 180 µl was then transferred to a new 0.5 ml collection tube, and 180 µl of 2X RIPA buffer (20 mM Tris pH 7.5, 2 mM EDTA, 2%Triton X-100, 0.2% SDS, 0.2% sodium deoxycholate, 200 mM NaCl/PIC) was added to recovered supernatants. A 1 /10 volume (36 µl) was removed for input control. ChIP-qualified H3K4me3 (Millipore #07-473) and H3K27me3 (Millipore #07-449) antibodies were added to the sonicated chromatin and incubated at 4°C overnight. Previously washed 10 µl of protein A magnetic beads (Invitrogen #88846) were added and incubated for additional 2 hours at 4°C. Immunoprecipitated complexes were washed three times with RIPA buffer and twice with TE (10 mM Tris pH 8.0/1 mM EDTA) buffer. Following transfer into new 1.5 ml collection tube, genomic DNA was eluted for 2 hours at 68 °C in 100 µl Complete Elution Buffer (20 mM Tris pH 7.5, 5 mM EDTA, 50 mM NaCl, 1% SDS, 50 µg/ml proteinase K), and combined with a second elution of 100

µl Elution Buffer (20 mM Tris pH 7.5, 5 mM EDTA, 50 mM NaCl) for 10 min at 68 °C. ChIPed DNA was purified by MinElute Purification Kit (Qiagen #28006) and eluted in 12 µl elution buffer. ChIP-seq libraries were prepared using ThruPLEX-DNA library preparation kit without extra amplification (Rubicon #R400406). Paired-end 100bp sequencing was performed on Illumina HiSeq 2500 platform. Sequenced reads were mapped to the mm9 mouse genome, and the distribution of chromatin features were analyzed by profile command of DANPOS.

Exome sequencing

Pooled genomic DNA isolated from control (n = 1), Tx-3 *Dnmt3a*^{KO} (n = 5) and Tx-12 *Dnmt3a*^{KO} (n = 2) HSCs were submitted to Otogenetics Corporation (Atlanta, GA, USA) for mouse exome capture and sequencing. Briefly, gDNA was subjected to agarose gel and OD ratio tests via Nanodrop to confirm the purity and concentration prior to Bioruptor (Diagenode Inc.) fragmentation. Fragmented gDNAs were tested for size distribution and concentration using an Agilent Tapestation 2200. Illumina libraries were made from qualified fragmented gDNA using SPRIworks HT Reagent Kit (Beckman Coulter, Inc. Indianapolis, IN USA, catalog# B06938) and the resulting libraries were subjected to exome enrichment using SureSelectXT Mouse All Exon (Agilent Technologies, Wilmington, DE USA, catalog# 5190-4641) following manufacturer's instructions. Enriched libraries were tested for enrichment by qPCR and for size distribution and concentration by an Agilent Bioanalyzer 2100. The samples were then sequenced on an Illumina HiSeq2500 which generated paired-end reads of 126 nucleotides (nt). Data was analyzed for data quality using FASTQC (Babraham Institute, Cambridge, UK). The raw fastq files were mapped against the mouse reference (GRCm38/mm10) using BWA-MEM (http://github.com/ih3/bwa). Subsequently, GATK SNP/indel Realigner were used to improve the final alignment and high-quality variants were filtered (GQ>20, minimum variant read count 10) and functionally annotated using snpEff.

TEL-seq

TEL-seq was used to estimate telomere lengths (Ding et al., 2014). TelSeq estimates telomere length by normalizing the number of telomeric motif reads by several factors such as library size. Since the estimations hinge on those factors, the authors of TelSeq recommended comparing estimated telomere lengths only within a single experiment. With this advice, we used the three exome sequence data sets (pooled genomic DNA isolated from control (n = 1), Tx-3 *Dnmt3a*^{KO} (n = 5) and Tx-12 *Dnmt3a*^{KO} (n = 2) HSCs) to perform TEL-seq analysis. Sequencing reads were aligned using bowtie2 version 2.2.7 with default parameters. Since their coverages are similar (Fig. S4E), TelSeq estimated telomere lengths (kB) from the exome sequencing data with default parameters.

Quantification and Statistical Analysis

Statistical analyses were performed to detect differences between the means of the conditions being compared. Statistical comparisons between groups were evaluated with Student's t-test or ANOVA as appropriate. All data are presented as mean ± standard error. Time to morbidity is presented in Kaplan-Meier survival curves and analyzed by Logrank test. Statistical analysis was performed using Prism 6 (Graphpad). Statistical significance is denoted as $*p<0.05$, $**p<0.01$, $***p<0.001$, *n* indicates the number of biological replicates within each group.

Data and Software Availability

Raw and processed WGBS, histone modification and RNA-sequencing data have been deposited to GEO under accession number GSE98191. UCSC Genome Browser tracks (mouse mm9) can be accessed from the hub http://lilab.research.bcm.edu/dldcc-web/lilab/hjpark/multipleTransplants/hub.txt. Exome sequencing data has been deposited to the NCBI sequence read archive (SRA) under accession number SRP133364.

SUPPLEMENTAL FIGURES

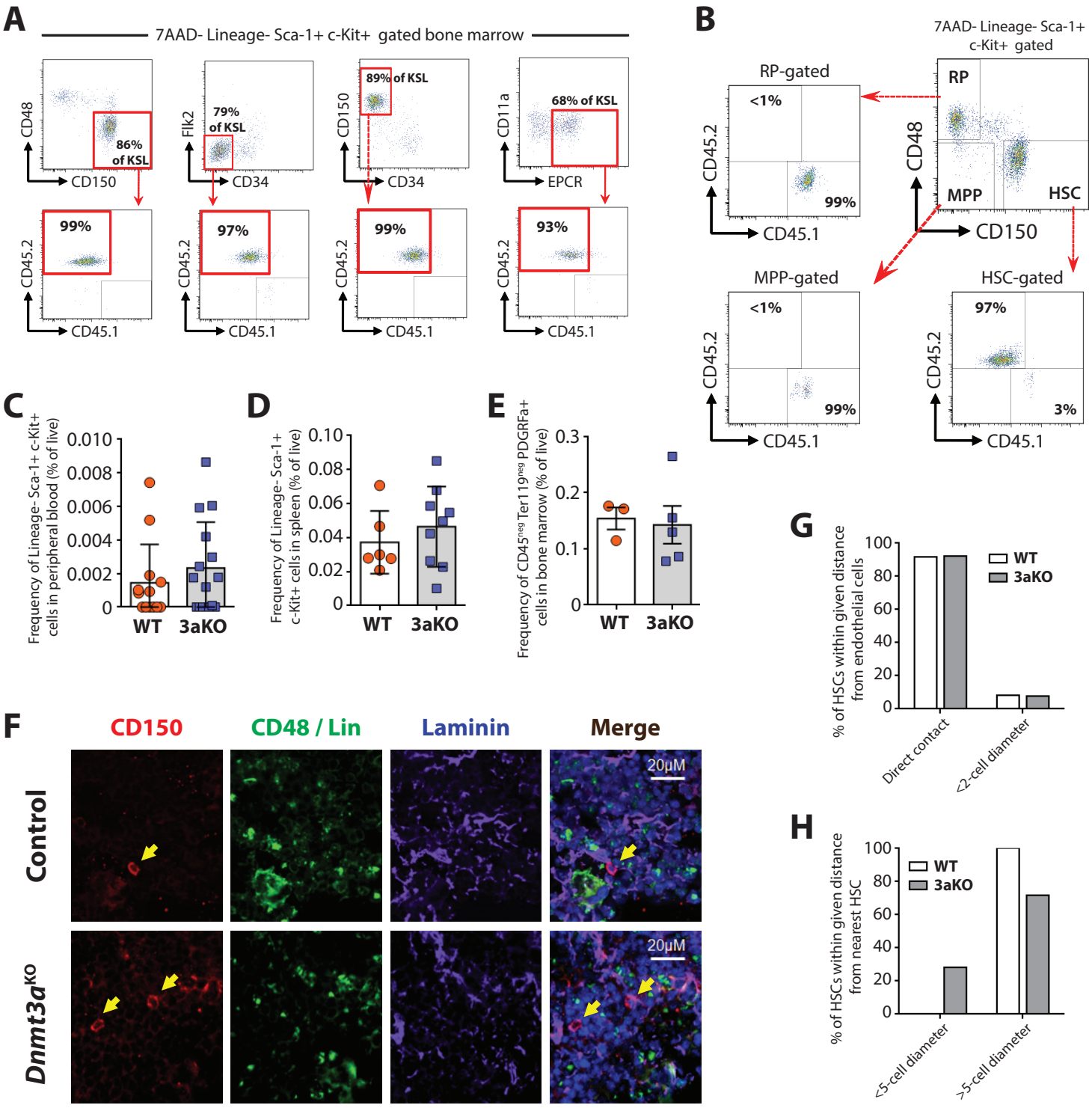
A
7AAD- Lineage- Sca-1+ c-Kit+ gated bone marrow
CD48
CD150
86% of KSL
99%
CD45.2
CD45.1
Flk2
CD34
79% of KSL
97%
CD150
89% of KSL
99%
CD11a
EPCR
68% of KSL
93%
B
7AAD- Lineage- Sca-1+ c-Kit+ gated
RP-gated
<1%
99%
RP
MPP
HSC
CD48
CD150
MPP-gated
<1%
99%
HSC-gated
97%
3%
C
Frequency of Lineage- Sca-1+ c-Kit+ cells in peripheral blood (% of live)
0.010
0.008
0.006
0.004
0.002
0
WT
3aKO
D
Frequency of Lineage- Sca-1+ c-Kit+ cells in spleen (% of live)
0.10
0.08
0.06
0.04
0.02
0
WT
3aKO
E
Frequency of CD45neg Ter119neg PDGRFa+ cells in bone marrow (% of live)
0.3
0.2
0.1
0
WT
3aKO
F
CD150
CD48 / Lin
Laminin
Merge
Control
Dnmt3aKO
20μM
20μM
G
% of HSCs within given distance from endothelial cells
100
80
60
40
20
0
WT
3aKO
Direct contact
<2-cell diameter
H
% of HSCs within given distance from nearest HSC
100
80
60
40
20
0
WT
3aKO
<5-cell diameter
>5-cell diameter

Figure S1: Loss of *Dnmt3a* provides HSCs with indefinite longevity. *Related to Figure 1*.

(A) Representative flow cytometry plots showing different schemes for prospective identification of Tx-11 *Dnmt3a*^{KO} HSCs. (B) Flow cytometry plot showing contribution of *Dnmt3a*^{KO} donor-derived cells to primitive progenitor cell fractions in a Tx-10 recipient mouse. HSC = hematopoietic stem cell, MPP = multipotent progenitor cell, RP = restricted progenitor. (C) Frequency of donor-derived hematopoietic progenitor cells (Lineage- Sca-1+ c-Kit+) in the peripheral blood of Tx-2 mice transplanted with control or *Dnmt3a*^{KO} HSCs. (D) Frequency of donor-derived hematopoietic progenitor cells (Lineage- Sca-1+ c-Kit+) in the spleen of Tx-2 mice transplanted with control or *Dnmt3a*^{KO} HSCs. (E) Frequency of bone marrow stromal cells in the bone marrow of mice transplanted with control or *Dnmt3a*^{KO} HSCs. (F) Immunohistochemical staining showing bone marrow localization of transplanted control and *Dnmt3a*^{KO} HSCs in Tx-3 mice. (G) Distribution of transplanted Tx-3 control and *Dnmt3a*^{KO} HSCs in the bone marrow in relation to endothelial cells. Data are from pooled analysis of slide sections representing three individual mice. (H) Spatial relationship of transplanted Tx-3 control and *Dnmt3a*^{KO} HSCs in relation to neighboring HSCs in the bone marrow. Data are from pooled analysis of slide sections representing three individual mice. Mean ± S.E.M. values are shown.

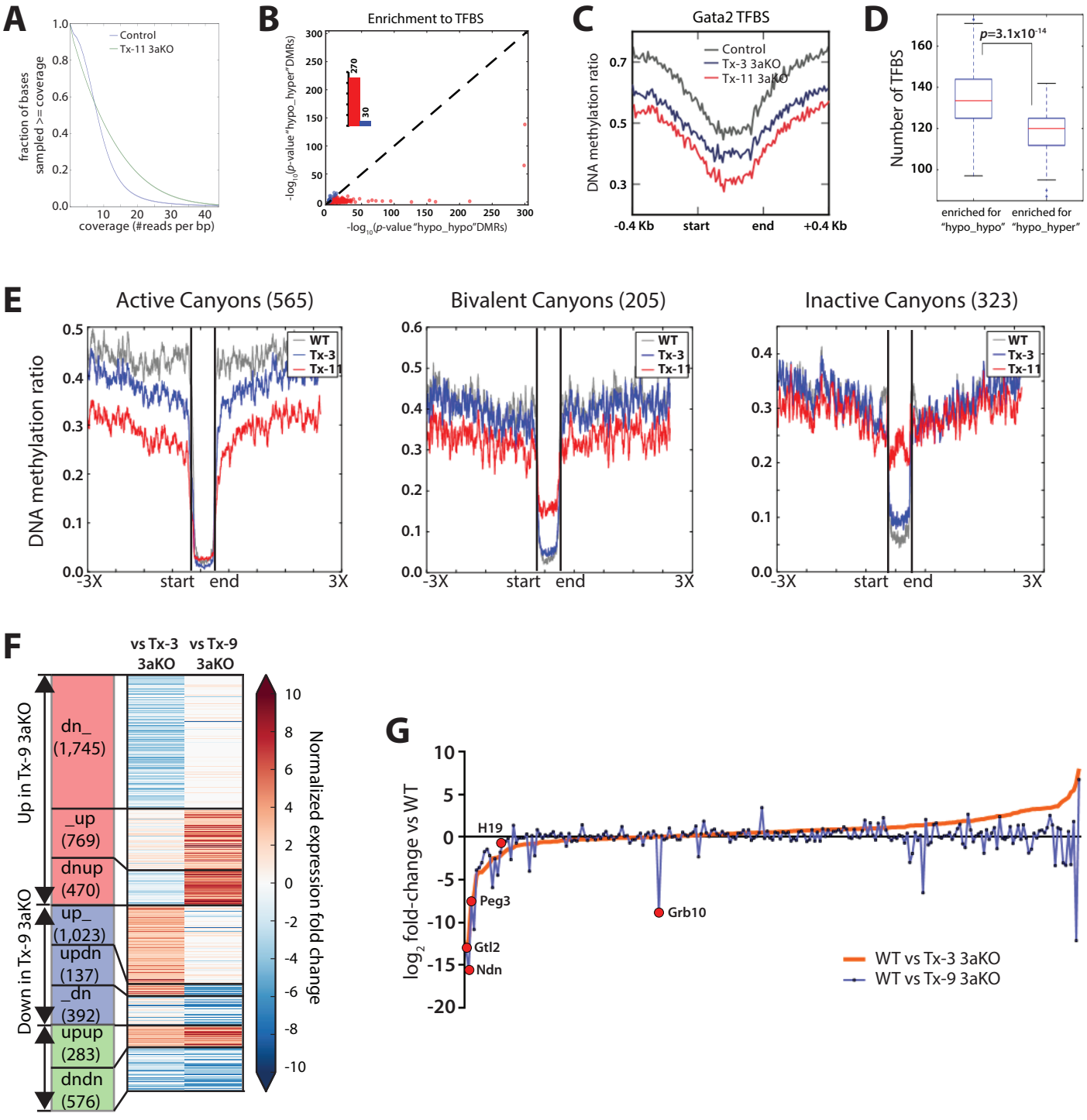
A
fraction of bases sampled >= coverage
coverage (#reads per bp)
Control
Tx-11 3aKO
B
Enrichment to TFBS
-log10(p-value "hypo_hyper" DMRs)
-log10(p-value "hypo_hypo" DMRs)
270
30
C
Gata2 TFBS
DNA methylation ratio
Control
Tx-3 3aKO
Tx-11 3aKO
-0.4 Kb
start
end
+0.4 Kb
D
Number of TFBS
p=3.1x10-14
enriched for "hypo_hypo"
enriched for "hypo_hyper"
E
Active Canyons (565)
Bivalent Canyons (205)
Inactive Canyons (323)
DNA methylation ratio
WT
Tx-3
Tx-11
-3X
start
end
3X
F
vs Tx-3 3aKO
vs Tx-9 3aKO
Up in Tx-9 3aKO
Down in Tx-9 3aKO
dn_ (1,745)
_up (769)
dnup (470)
up_ (1,023)
updn (137)
_dn (392)
upup (283)
dndn (576)
Normalized expression fold change
G
log2 fold-change vs WT
H19
Peg3
Gtl2
Ndn
Grb10
WT vs Tx-3 3aKO
WT vs Tx-9 3aKO

Figure S2: Dnmt3a controls DNA methylation at HSC regulatory elements. *Related to Figure 2*.

(A) Coverage of the whole genome bisulfite sequencing data. (B) Enrichment of "hypo_hypo" (red) and "hypo_hyper" (blue) DMRs for 300 sets of binding sites for 254 transcription factors found in 11 mouse cell types. (C) Average DNA methylation level of *Gata2* binding sites throughout the genome of HSCs of the indicated genotype/transplant-stage. (D) Enrichment of "hypo_hypo" and "hypo_hyper" DMRs for TFBS from 100 random computational samplings of 600 DMRs within each category. (E) DNA methylation levels of active, bivalent, and inactive canyons in control (WT), Tx-3 *Dnmt3a*^{KO} (Tx-3), and Tx-11 *Dnmt3a*^{KO} (Tx-11) HSCs. Flanking regions are extended by three-fold length as the corresponding canyon regions (±3X). (F) Heatmap showing expression fold change of genes from control HSCs to Tx-3 *Dnmt3a*^{KO} and Tx-9 *Dnmt3a*^{KO} HSCs that are up-regulated (up), down-regulated (dn) or not differentially expressed (_) within each comparison. (G) Distribution of expression fold change of HSC fingerprint genes in Tx-3 and Tx-9 *Dnmt3a*^{KO} HSCs relative to control HSCs ranked by fold change in Tx-3 *Dnmt3a*^{KO} HSCs. Imprinted genes are highlighted.

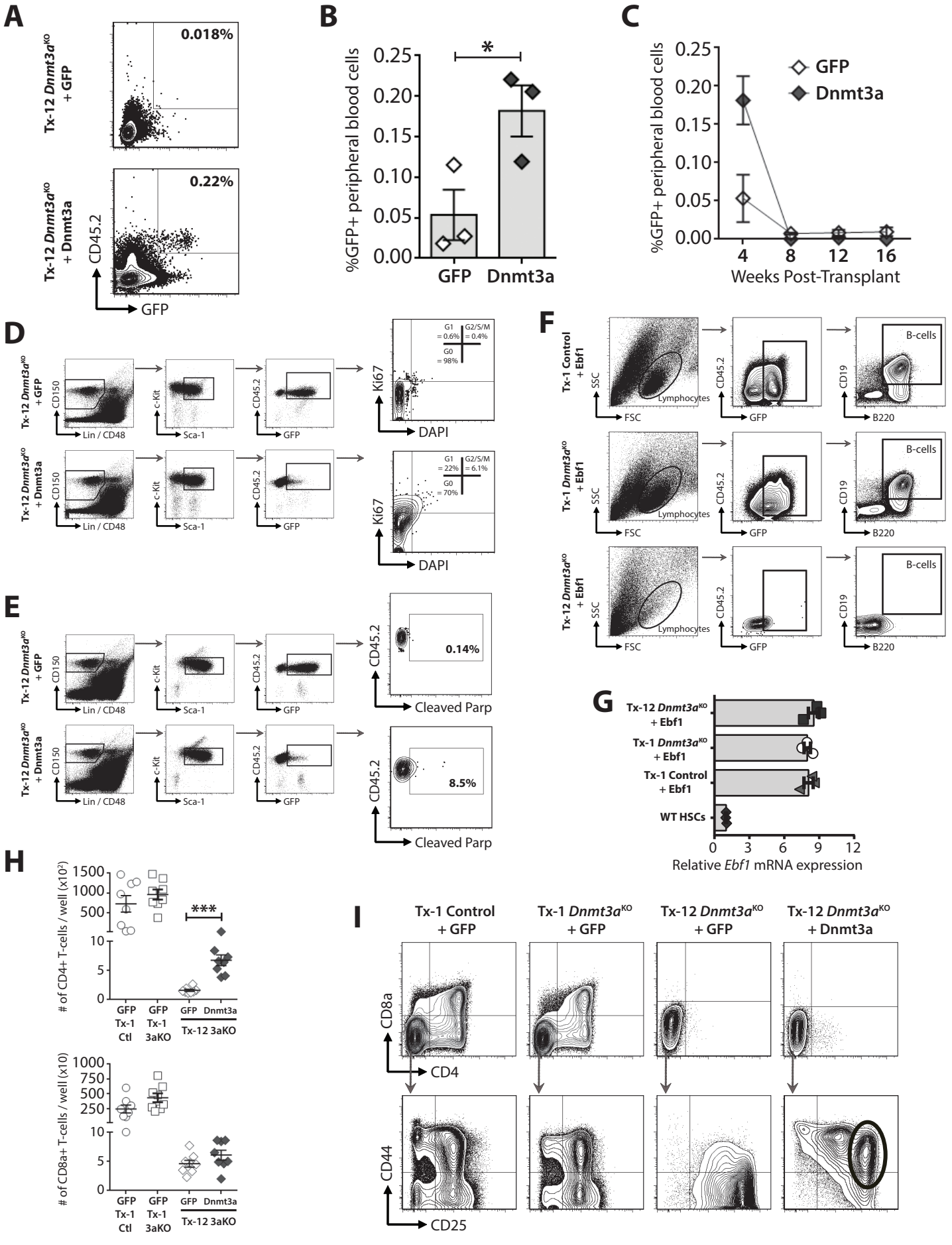
A
Tx-12 Dnmt3a^KO + GFP
0.018%
Tx-12 Dnmt3a^KO + Dnmt3a
0.22%
CD45.2
GFP
B
%GFP+ peripheral blood cells
0.25
0.20
0.15
0.10
0.05
0.00
*
GFP
Dnmt3a
C
%GFP+ peripheral blood cells
GFP
Dnmt3a
4
8
12
16
Weeks Post-Transplant
D
Tx-12 Dnmt3a^KO + GFP
CD150
Lin / CD48
c-Kit
Sca-1
CD45.2
GFP
Ki67
DAPI
G1 = 0.6%
G2/S/M = 0.4%
G0 = 98%
Tx-12 Dnmt3a^KO + Dnmt3a
G1 = 22%
G2/S/M = 6.1%
G0 = 70%
E
0.14%
8.5%
Cleaved Parp
F
Tx-1 Control + Ebf1
Tx-1 Dnmt3a^KO + Ebf1
Tx-12 Dnmt3a^KO + Ebf1
SSC
FSC
Lymphocytes
B-cells
CD19
B220
G
Tx-12 Dnmt3a^KO + Ebf1
Tx-1 Dnmt3a^KO + Ebf1
Tx-1 Control + Ebf1
WT HSCs
0
3
6
9
12
Relative Ebf1 mRNA expression
H
# of CD4+ T-cells / well (x10²)
1500
1000
500
10
5
0
***
GFP Tx-1 Ctl
GFP Tx-1 3aKO
GFP
Dnmt3a
Tx-12 3aKO
# of CD8a+ T-cells / well (x10)
1000
750
500
250
10
5
0
I
Tx-1 Control + GFP
Tx-1 Dnmt3a^KO + GFP
Tx-12 Dnmt3a^KO + GFP
Tx-12 Dnmt3a^KO + Dnmt3a
CD8a
CD4
CD44
CD25

Figure S3: Differentiation capacity is lost but transformation potential retained in immortalized *Dnmt3a*^{KO} HSCs. *Related to Figure 3*.

(A) Flow cytometry plot showing GFP+ cells in blood of mice transplanted with Tx-11 *Dnmt3a*^{KO} HSCs transduced with control (GFP) or *Dnmt3a*-expressing (Dnmt3a) lentivirus four-weeks post-transplant. (B) Frequency of GFP+ cells in peripheral blood of mice transplanted with Tx-11 *Dnmt3a*^{KO} HSCs transduced with control (GFP) or *Dnmt3a*-expressing (Dnmt3a) lentivirus four-weeks post-transplant. (C) Contribution of transduced Tx-11 *Dnmt3a*^{KO} HSCs to peripheral blood chimerism over time. (D) Flow cytometry plots showing HSC cell cycle analysis. (E) Flow cytometry plots showing HSC apoptosis analysis. (F) Flow cytometry analysis of B-cell differentiation after 14-days *in vitro*. (G) Expression level of *Ebf1* in HSCs following lentiviral (+Ebf1) transduction. (H) Quantification of T-cells after 28-day culture on OP9-DL1 stromal cells. (I) Flow cytometry plots of T-cell analysis after 28-days. Circle denotes an anomalous $CD4^{-}CD8a^{-}CD44^{+}CD25^{bright}$ population following over-expression of *Dnmt3a*. **p*<0.05, ****p*<0.001. Mean ± S.E.M. values are shown.

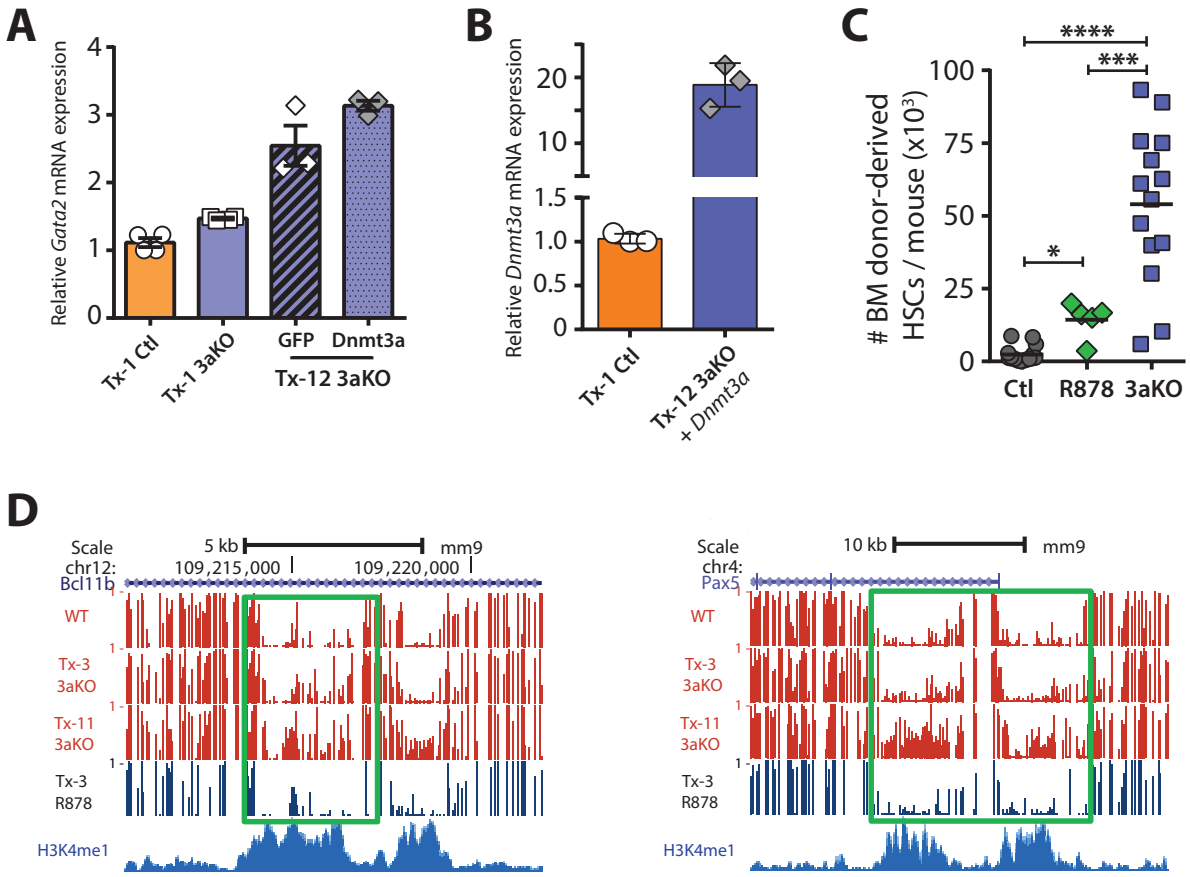

E

	Total Reads	Mapped Reads	Telomere Length
Control	52.3K	51.6K	0.232326
Tx-3 3aKO	45.3K	45.1K	0.227738
Tx-12 3aKO	42.9K	42.6K	0.227643

Figure S4: Molecular Analysis of Dnmt3a Rescue, Dominant-Negative Mutant, and Clonal Hematopoiesis. *Related to Figure 4*.

(A) Expression level of *Gata2* in Tx-12 *Dnmt3a*^{KO} HSCs transduced with control (GFP) or *Dnmt3a*-expressing (Dnmt3a) lentivirus compared to other HSC genotypes/transplant-stages. (B) *Dnmt3a* expression level in Tx-12 *Dnmt3a*^{KO} (3aKO) HSCs rescued with *Dnmt3a*-expressing lentivirus compared to control (Ctl) HSCs. (C) Number of donor-derived HSCs in the bone marrow of Tx-3 mice transplanted with control, *Dnmt3a*^{R878} and *Dnmt3a*^{KO} HSCs. (D) WGBS profiles showing hypermethylation of enhancer regions of lineage-specific differentiation genes *Bcl11b* and *Pax5* in *Dnmt3a*^{KO} HSCs (green boxes) is not observed in *Dnmt3a*^{R878} HSCs. (E) Statistics from Tel-seq analysis of telomere length (kB) in indicated HSC genotypes. ***p<0.001, ****p<0.0001. Mean ± S.E.M. values are shown.

RESOURCE TABLE

REAGENT or RESOURCE	SOURCE	IDENTIFIER
Antibodies		
BV605 anti-mouse CD45.2	Biolegend	109841
FITC anti-mouse CD45.1	Biolegend	110706
APCy7 anti-mouse Gr-1	Biolegend	108424
APCy7 anti-mouse Mac-1	Biolegend	101226
APCy7 anti-mouse B220	Biolegend	103224
APCy7 anti-mouse CD3e	Biolegend	100330
APCy7 anti-mouse Ter119	Biolegend	116223
BV421 anti-mouse c-Kit	Biolegend	84158
APC anti-mouse Sca-1	Biolegend	122512
PECy7 anti-mouse CD48	Biolegend	103424
PE anti-mouse CD150	Biolegend	115904
BV421 anti-mouse CD45.2	Biolegend	84208
APC anti-mouse CD3e	Biolegend	100312
APC anti-mouse B220	Biolegend	103212
PECy7 anti-mouse Gr-1	Biolegend	108416
PECy7 anti-mouse Mac-1	Biolegend	101216
PECy7 anti-mouse B220	Biolegend	103222
FITC anti-mouse CD45.1	Biolegend	110706
PE anti-mouse CD25	eBioscience	12-0251-83
PECy7 anti-mouse CD8	BD Biosciences	552877
APC anti-mouse CD4	eBioscience	17-0041-81
PECy7 anti-mouse CD19	BD Biosciences	552854
BV605 anti-mouse Ki67	BioLegend	652413
PE anti-cleaved Parp	BD Biosciences	552933
FITC anti-mouse CD11b	eBioscience	11-0112-82
PE anti-mouse CD11a	Biolegend	101107
PE anti-mouse Flk2	BD Biosciences	553842
APC anti-mouse CD34	Biolegend	119310
APC anti-mouse EPCR	Biolegend	14156
BV605 anti-mouse CD45.1	Biolegend	110738
APCy7 anti-mouse CD44	Biolegend	103028
PE anti-mouse CD25	eBioscience	12-0251-83
PECy7 anti-mouse CD8a	BD Biosciences	552877
APC anti-mouse CD4	eBioscience	17-0041-81
Chemicals, Peptides, and Recombinant Proteins		
Polyinosinic-polycytidylic ribonucleic acid (pIpC)	Sigma	p1530
Pen/Strep	Fisher Scientific	MT30002CI
HEPES	Life Technologies	15630080
Fetal Bovine Serum (FBS)	Sigma	14009C
Polyethylenimine (PEI)	Polysciences	23966-1
L-glutamine	Corning	25-005-CI
Polybrene	Sigma	TR-1003-G

Recombinant murine stem cell factor (SCF)	Thermo Fisher Scientific	PMC2111
Recombinant murine thrombopoietin (TPO)	Thermo Fisher Scientific	PMC1141
Recombinant murine Flt3L	Miltenyl Biotec	130-097-372
Recombinant murine interleukin-3 (IL-3)	Miltenyl Biotec	130-099-508
Recombinant murine interleukin-7 (IL-7)	Miltenyl Biotec	130-094-066
Critical Commercial Assays		
Methocult 3434 medium	Stem Cell Technologies	03434
BD Cytofix/Cytoperm	BD Biosciences	554714
Deposited Data		
RNAseq	This study	GEO: GSE98191
ChIPseq	This study	GEO: GSE98191
Experimental Models: Cell Lines		
OP9 cells	ATCC	CRL-2749
OP9-DL1 cells	Schmitt *et al*., 2002	N/A
Experimental Models: Organisms/Strains		
Mx1-Cre	Kuhn *et al*., 1995	N/A
Dnmt3a fl/fl	Kaneda *et al*., 2004	N/A
C57Bl/6 CD45.1	The Jackson Laboratory	002014
Oligonucleotides		
Primer Name	**Sequence (5'->3')**	
*Kras*_Forw	atatatggcgcgccatgactgagtataagcttgtggt	IDT
*Kras*_Rev	atatatctcgagttacataactgtacaccttgtccttg	IDT
*Dnmt3a*_Forw	atacatggcgcgccatgccctccagcggccccgg	IDT
*Dnmt3a*_Rev	atgtatctcgagttacacacaagcaaaatattccttcag	IDT
*Ebf1*_Forw	atatataggcgcgccatgtttgggatccaggaaagcat	IDT
*Ebf1*_Rev	atatatatgcatgctcacatgggagggacaatca	IDT
Recombinant DNA		
Dnmt3a cDNA	Open Biosystems	BC007466
Ebf1 cDNA	Addgene	96965
Kras cDNA	Origene	NM_021284
Software and Algorithms		
PRISM (version 6)	GraphPad Software	N/A
FlowJo (version 10)	https://www.flowjo.com	N/A
IGV	https://www.broadinstitute.org	N/A
Partek Genomics Suite 6.6	http://www.partek.com/pgs	N/A
SeqBuilder14	https://www.dnastar.com/	N/A
Python (version 2.7)	https://www.python.org	N/A
Numpy (version 1.9.2)	http://www.numpy.org/	N/A
R (version 3.4.2)	https://www.r-project.org/	N/A
deepTools (version 2.4.2)	http://deeptools.readthedocs.io/en/latest/	N/A

Taqman expression assays for RT-qPCR		
Bax	Mm00432051_m1	4331182
Bbc3	Mm00519268_m1	4331182
Gata2	Mm00492301_m1	4331182

Sequencing Reagents		
TruSeq Stranded Total RNA Library Kit	Illumina	RS-122-2101
Truseq DNA methylation Kit	Illumina	EGMK81312
ThruPlex DNA library preparation Kit	Rubicon	R400406
NextSeq 500 mid output kit	Illumina	FC-404-2001
PureLink Genomic DNA mini kit	Invitrogen	K182001
KAPA library quantification kit	Kapa Biosystem	KK4844
ChIP qualified Antibodies and reagents		
H3K4me3	Millipore	07-473
H3K27me3	Millipore	07-449
H3K4me1	Abcam	Ab8895
Protein A magnetic beads	Invitrogen	88846